

RESEARCH

Open Access



# The HNRNPC/CELF2 signaling pathway drives glycolytic reprogramming and mitochondrial dysfunction in drug-resistant acute myeloid leukemia

Xiang Ma<sup>1</sup>, Haodong Li<sup>1</sup>, Ziqi Zhao<sup>2</sup>, Changchun Li<sup>2</sup>, Man Wang<sup>1</sup>, Lele Zhang<sup>1</sup>, Yutong Zhao<sup>1</sup>, Haipeng Su<sup>1</sup>, Feng Wang<sup>2</sup> and Jiai Hua<sup>1,2\*</sup>

## Abstract

**Background** Acute myeloid leukemia (AML) is an aggressive cancer with high treatment resistance, often leading to poor patient outcomes. Metabolic reprogramming plays a critical role in AML progression, influencing drug resistance (DR) and tumor survival. This study investigates the HNRNPC/CELF2 signaling pathway and its impact on AML cell metabolism and DR.

**Results** The study identified that HNRNPC regulates the expression of CELF2 through m6A modification. In drug-resistant AML cells, increased HNRNPC expression and decreased CELF2 expression were associated with upregulated glycolysis, enhanced glucose consumption, lactate production, and mitochondrial dysfunction. Knockdown of HNRNPC reduced glycolysis and cell invasion, while CELF2 knockdown reversed these effects. Conversely, HNRNPC overexpression enhanced glycolysis and cell migration, which were counteracted by CELF2 overexpression.

**Conclusions** The HNRNPC/CELF2 axis plays a pivotal role in metabolic reprogramming, driving AML progression and chemotherapy resistance. Targeting this pathway may offer new therapeutic strategies to overcome resistance and improve treatment outcomes in AML patients.

**Keywords** Acute myeloid leukemia, Heterogeneous nuclear ribonucleoprotein C, CUGBP elav-like family member 2, Glucose metabolism reprogramming, Drug resistance, Cell migration

## Introduction

Acute myeloid leukemia (AML) is a malignant tumor originating from abnormal proliferation of hematopoietic stem cells in the bone marrow [1, 2]. The prognosis for

AML patients remains poor due to treatment resistance and disease progression [3, 4]. Therefore, gaining a deep understanding of the molecular mechanisms of AML is crucial for improving patients' survival rates and treatment outcomes. The pathogenesis of AML is not fully understood, but studies have suggested that aberrant gene expression and activation of abnormal signaling pathways within cells may be involved in the development and progression of AML [5–7].

HNRNPC and CELF2 are both RNA-binding proteins that have been identified as key genes in AML cells [8]. While HNRNPC plays a significant role in various

\*Correspondence:

Jiai Hua

huaja@tit.edu.cn

<sup>1</sup> Laboratory of Biochemistry and Pharmacy, Taiyuan Institute of Technology, No. 31, Xinlan Road, Jiancaoping District, Taiyuan 030008, Shanxi, People's Republic of China

<sup>2</sup> Chemistry and Chemical Engineering Department, Taiyuan Institute of Technology, Taiyuan 030008, People's Republic of China



© The Author(s) 2025. **Open Access** This article is licensed under a Creative Commons Attribution-NonCommercial-NoDerivatives 4.0 International License, which permits any non-commercial use, sharing, distribution and reproduction in any medium or format, as long as you give appropriate credit to the original author(s) and the source, provide a link to the Creative Commons licence, and indicate if you modified the licensed material. You do not have permission under this licence to share adapted material derived from this article or parts of it. The images or other third party material in this article are included in the article's Creative Commons licence, unless indicated otherwise in a credit line to the material. If material is not included in the article's Creative Commons licence and your intended use is not permitted by statutory regulation or exceeds the permitted use, you will need to obtain permission directly from the copyright holder. To view a copy of this licence, visit <http://creativecommons.org/licenses/by-nc-nd/4.0/>.

cancers, its role in AML remains unclear [9–11]. CELF2 is a transcription factor involved in selective splicing and gene expression regulation in cells [8]. HNRNPC regulates the selective splicing of CELF2 through m6A modification, thereby further influencing the biological characteristics of AML cells [10, 12, 13].

The research has discovered that HNRNPC promotes the proliferation, migration, and infiltration of AML cells by inhibiting CELF2 [8]. In addition, HNRNPC also regulates the glycolytic reprogramming of AML cells, affecting the expression of glycolysis-related genes and cellular energy metabolism [14–17]. This research further reveals the crucial role of the HNRNPC/CELF2 signaling pathway in AML, providing a new perspective for understanding the development mechanisms of AML.

Treatment resistance is one of the main challenges in current AML therapy [18]. The research has found that glycolysis plays an important role in tumor progression and resistance [19, 20]. The findings of this study provide new targets for the development of therapeutic strategies based on HNRNPC or CELF2, which could potentially improve existing AML treatment methods. Additionally, studying the role of the glycolytic pathway in AML drug resistance (DR) may offer new treatment approaches to overcome resistance.

In conclusion, this study aims to provide new insights into addressing treatment resistance in AML by elucidating the roles of the HNRNPC/CELF2 signaling pathway in tumor progression and glycolytic reprogramming. The scientific and clinical significance of these research findings is essential for improving the prognosis of AML patients. This discovery lays the foundation for future development of therapeutic strategies targeting HNRNPC or CELF2, offering the potential for more effective treatment options for AML patients, as well as providing insights for the study of other leukemias and tumors. By gaining a deep understanding of the molecular mechanisms of AML and treatment resistance, new approaches and methods for personalized precision therapy can be developed, ultimately improving patients' quality of life and long-term survival rates.

## Results

### Leukemia biomarkers are significantly elevated in drug-resistant AML mice compared to non-resistant mice

AML is a prevalent and highly deadly type of acute leukemia in adults. Its biological features are primarily characterized by the invasive proliferation of primitive, immature white blood cells (blast cells) in the bone marrow, peripheral blood, and other tissues, accompanied by hindered cell differentiation and dysregulated apoptosis [21]. Refractory AML, a more challenging type of AML

for treatment, poses a significant challenge in the field of hematological malignancies due to its resistance to chemotherapy, severe treatment complications, and high relapse rate [22].

In this study, we initially subjected mice to sublethal whole-body irradiation (450 cGy) to suppress their bone marrow hematopoietic function [22]. Subsequently, we established an AML mouse model by tail vein injection of C1498 AML cells expressing ZsGreen1 fluorescent protein (Figure S1 A), which possesses low immunogenicity *in vivo* [23]. On the 14th day of the experiment, we observed a significant decrease in body weight in the AML group compared to the control group (Figure S1B). By analyzing peripheral blood leukocyte (WBC), red blood cell (RBC), and platelet (PLT) counts, we found a significant increase in WBC count and a decrease in RBC and PLT counts in AML mice (Figure S1 C).

On the 14th day, we administered intraperitoneal Cytarabine (dose: 3 mg/kg/day). After a week of treatment, we observed treatment effects in most mice, with an increase in body weight, a decrease in peripheral blood leukocyte count, and an increase in RBC and PLT counts (Figure S1D-F). However, after two additional weeks of continued treatment, we noticed a sustained weight loss in a minority of mice. Consequently, we reexamined the peripheral blood of mice in the weight loss group ( $n = 6$ ) and weight gain group ( $n = 10$ ), revealing a continued increase in WBC count and a decrease in RBC and PLT counts in AML mice with weight loss (Figure S1G-I). Therefore, we defined the weight loss group as the drug-resistant group (DR) and the weight gain group as the drug sensitive group (DS) and six animals were assigned to each group for further experiments.

Furthermore, we assessed the expression of leukemia cell markers CD11b, CD41a, and Ter119 in isolated bone marrow cells from AML mice using flow cytometry and immunofluorescence staining. We also analyzed their mean fluorescence intensity (MFI). The results showed significantly higher expression levels of leukemia markers in the drug-resistant group compared to the drug-sensitive group (Figure S1 J).

Consequently, we successfully identified drug-resistant mice and drug-sensitive mice.

### Increased interaction strength among bone marrow immune cells in drug-resistant AML mice compared to non-resistant mice

To determine the heterogeneity of DR and DS mouse bone marrow cells in AML, we performed single-cell transcriptome sequencing (scRNA-seq) analysis on DR and DS mouse bone marrow cells. The data was integrated using the Seurat package. Most cells had  $n\text{Feature\_RNA} < 5000$ ,  $n\text{Count\_RNA} < 20000$ , and  $\text{percent.mt}$

< 20% (Figure S2 A). After filtering low-quality cells based on these criteria, we obtained an expression matrix containing 14,432 genes and 55,719 cells. Analysis showed a correlation coefficient of  $-0.08$  between nCount\_RNA and percent. Mt, and a correlation coefficient of  $0.95$  between nCount\_RNA and nFeature\_RNA (Figure S2B), indicating the filtered cell data was of good quality for further analysis.

Next, we selected 2000 highly variable genes based on expression variance (Figure S2 C). The cell cycle was calculated using the CellCycleScoring function (Figure S2D), and the data was normalized. PCA was then used for linear dimensionality reduction (Figure S2E), and the distribution of cells on PC\_1 and PC\_2 was visualized (Figure S2 F). The results revealed the presence of batch effects between samples.

To eliminate batch effects and improve the accuracy of cell clustering, we performed batch correction using the harmony package (Figure S3 A). Additionally, we sorted the principal components (PCs) based on their standard deviation using the ElbowPlot (Figure S3B). The results of batch correction showed effective removal of batch effects (Figure S3 C).

Subsequently, we performed non-linear dimensionality reduction using the UMAP algorithm on the top 20 principal components and visualized the clustering at different resolutions using the cluster package (Figure S4). Based on the UMAP clustering analysis, we identified 26 cell clusters (Figure S3D–E).

First, we annotated 8 cell types based on marker genes (Figure S3 F; Fig. 1A). To better extract AML cells, we inferred the large-scale chromosome copy number variations (CNVs) in the remaining cells (16 clusters) using the InferCNV tool (Fig. 1B). Using T cells, macrophages, fibroblasts, cDC cells, plasma cells, monocytes, and B cells as reference cells, we found that Cluster 1, 3, 6, 11, and 13 exhibited higher variability compared to other cells (Fig. 1C). Therefore, we defined Cluster 1, 3, 6, 11, and 13 in the rest of the myeloid cells as AML cells and further annotated the remaining cells as GMPs (granulocyte–macrophage progenitors), CMPs (common myeloid progenitors), and granulocytes based on marker genes (Fig. 1D–F). We further analyzed the proportion of re-annotated cells in each sample (Fig. 1G) and found a

significant increase in AML cells in the DR group, while immune cells, such as T cells, increased significantly in the non-resistant group (Figure S3G).

To investigate the pathway activities between different cell types, we utilized the "CellChat" package developed in R. The analysis showed significant differences in cell–cell communication activity between the DR and DS groups. Specifically, the communication intensity between cells in the DR group was relatively higher (Fig. 1H). In the DR group, the interaction strength between AML cells and macrophages, as well as T cells, was higher compared to the DS group (Figure S5 A).

Furthermore, comparing the total number and intensity of signaling pathway interactions between the DS and DR groups, we found that although the DR group had a lower number of interactions, the intensity of interactions was higher (Figure S5B). Additionally, we observed a notable increase in the number and intensity of interactions between AML cells and macrophages, monocytes, and other cells in the DR group (Figure S5 C).

In subsequent analysis, we focused on the AML cell population and performed re-annotation. Using the "Monocle2" package, we conducted pseudotime analysis to reveal the migration trajectory of cells and the composition of different clusters in pseudotime (Figure S5D). Combining the UMAP plot and pseudotime analysis, we classified AML cells into three different differentiation stages, namely Stage 1–3 (Figure S5E–F). By calculating the proportions of cells in three stages in both groups, we found a significantly higher proportion of cells in Stage 3 in the DR group compared to the DS group (Figure S5G–H), which may reflect the differentiation characteristics of AML cells during the development of DR.

Based on the above research, we successfully identified 11 cell types in the scRNA-seq dataset and found increased interaction intensity between AML cells and various immune cells in the DR group.

#### **iTRAQ analysis reveals differentially expressed proteins in AML cells primarily enriched in redox processes, redox coenzyme metabolism, and glycolysis**

Through scRNA-seq analysis, we uncovered significant connections between AML cells and immune cells such as macrophages and T cells. To further identify key genes

(See figure on next page.)

**Fig. 1** Single-cell transcriptome sequencing reveals microscale changes in cell populations in bone marrow tissue. **A** Schematic diagram of the single-cell transcriptome sequencing process; **B** Visualization of cell annotation results based on UMAP clustering; **C** InferCNV analysis displaying copy number variation and deletions, with T cells, macrophages, fibroblasts, cDC cells, plasma cells, monocytes, and B cells as reference cells; **D** UMAP plot showing the expression of GMP, CMP, and granulocyte marker genes; **E** Heatmap of the top three correlated genes in each annotated AML cell; **F** UMAP visualization of annotated AML cells; **G** Cell proportions of the 11 cell types in each sample; **H** Cell communication network in the samples, with line thickness representing pathway numbers on the left and interaction strength on the right

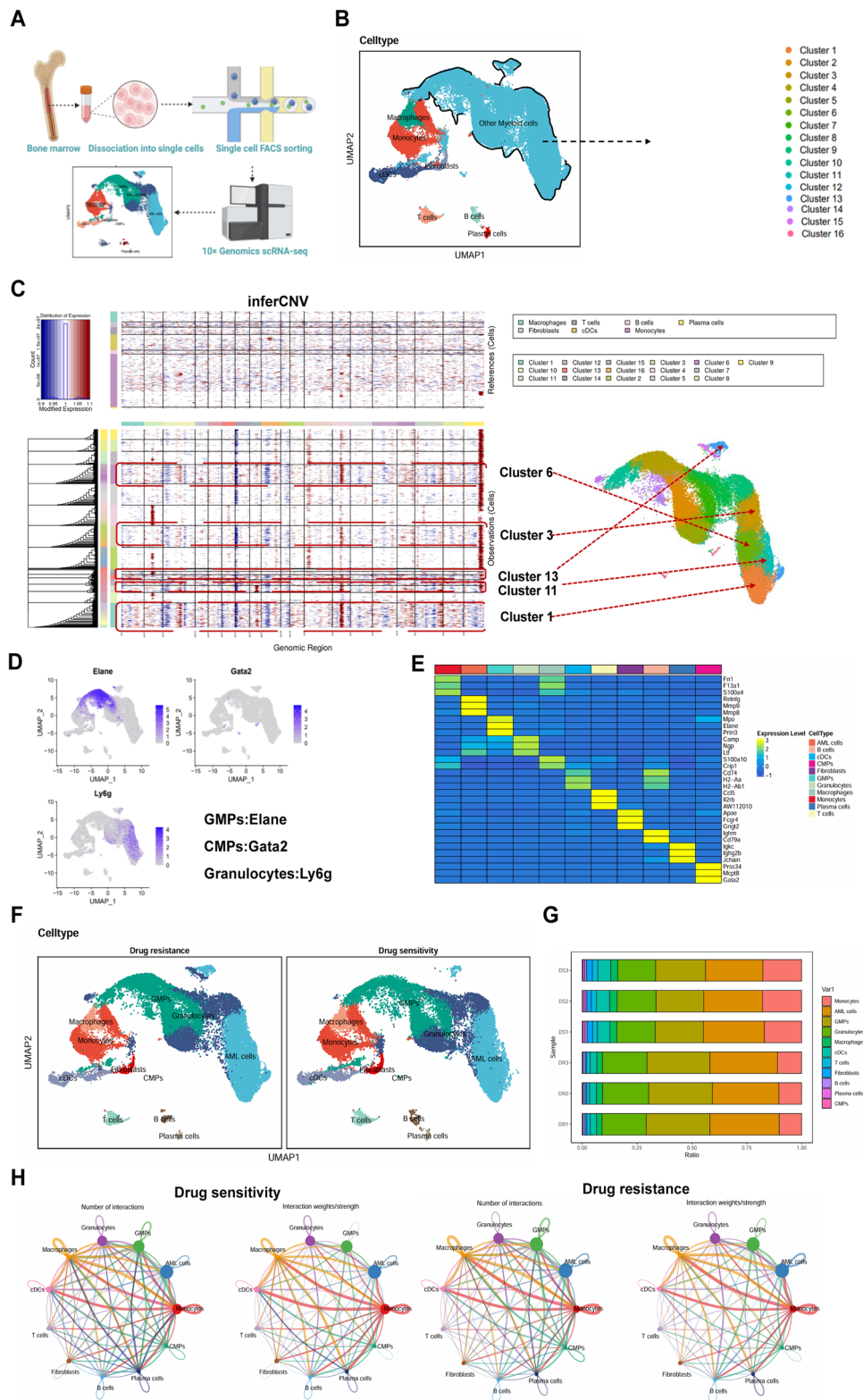


**Fig. 1** (See legend on previous page.)

regulating AML cells, we employed isobaric tags for relative and absolute quantification (iTRAQ) technology combined with mass spectrometry analysis to perform quantitative analysis on the proteome of drug-resistant (DR) and drug-sensitive (DS) bone marrow samples. Principal component analysis (PCA) revealed distinct differences in protein expression profiles among the different groups (Fig. 2A). Further analysis indicated that the expression patterns of proteins with different molecular weights were similar between the two groups (Fig. 2B). We detected a total of 2,756 proteins in the bone marrow tissue, with more than 50% of these proteins having a sequence coverage exceeding 10% (Fig. 2C). Moreover, more than half of the proteins covered three or more peptide segments, further validating the high quality and reliability of the identified proteins (Fig. 2D).

In the DS and DR groups, a total of 205 differentially expressed proteins (DEPs) were identified, with 116 proteins upregulated and 89 proteins downregulated (Fig. 2E). We also performed cluster analysis on the top 50 ranked DEPs to better understand the differences in their expression patterns (Fig. 2F).

Functional enrichment analysis of the differentially expressed proteins using Gene Ontology (GO) revealed their involvement in important biological processes such as oxidative-reduction processes, oxidative-reduction coenzyme metabolic processes, and glucose catabolic processes. These proteins were found to function in molecular compartments such as cytosol, extracellular vesicles, and lysosomes. Significant changes were observed in the activity of oxidative-reduction enzymes and their roles as aldehyde or hydroxyl donors (Fig. 2G).

By conducting KEGG pathway enrichment analysis, we identified significant alterations in pathways such as the PI3 K-Akt signaling pathway, AML, glycolysis/gluconeogenesis, and the PD-L1 expression and PD-1 checkpoint pathways in tumors (Fig. 2H).

Using the iTRAQ technology, we conducted a comprehensive quantitative analysis of the proteome in drug-resistant and drug-sensitive bone marrow samples. The discovery of differentially expressed proteins and the functional enrichment analysis sheds further light on the critical roles of these proteins in oxidative-reduction processes, oxidative-reduction coenzyme metabolism, and glucose catabolic processes.

#### **HNRNPC-mediated m6 A modification suppresses CELF2 splicing and causes DR in AML cells**

In order to accurately identify key genes regulating DR in AML cells, we first performed differential gene analysis on a scRNA-seq dataset of AML cell populations. The analysis revealed a total of 488 differentially expressed genes (DEGs), with 206 genes significantly upregulated

and 282 genes significantly downregulated (Fig. 3A). Subsequently, we compared these DEGs with differentially expressed proteins (DEPs) identified through proteomic methods and found 18 intersecting genes using a Venn diagram visualization (Fig. 3B). We further conducted a protein-protein interaction (PPI) network analysis of these 18 intersecting genes using the String database (<https://cn.string-db.org/>). Based on our previous research associating HNRNPC with AML progression (client-associated order SE-23-016), we noticed an interaction between HNRNPC and CELF2 and FUS (Fig. 3C).

Building on this analysis, we examined the expression levels of HNRNPC, CELF2, and FUS in both the scRNA-seq dataset and the proteomic dataset. Our results revealed inconsistent expression trends for FUS in the two datasets (Fig. 3D, E). Furthermore, we performed pseudo-time analysis on AML cells from the drug-resistant group (DR group) and observed that Stage 3 cells were more concentrated in the later stages of analysis (Fig. 3F). Upon further examination of the expression fluctuations of HNRNPC and CELF2 genes, we discovered that CELF2 expression initially increased and then decreased, whereas HNRNPC expression followed the opposite trend, decreasing initially and then increasing (Fig. 3G).

Previous studies have shown that HNRNPC promotes tumor cell proliferation and migration, facilitating the progression of various cancers [9, 24] as well as the proliferation of chronic lymphocytic leukemia cells [25]. On the other hand, CELF2 has been found to suppress tumor growth in AML [26, 27].

Currently, HNRNPC is known as a splicing inhibitor that suppresses alternative splicing events by recognizing and binding to splicing silencer sequences on pre-mRNA [28]. The M6a2 target database (<http://rm2target.canceromics.org/#/home>) validated CELF2 as a substrate for HNRNPC in the THP1 cell line (Figure S6 A).

Based on these findings, we hypothesize that in AML cells, HNRNPC may inhibit CELF2 splicing through m6 A modification, thereby leading to DR.

#### **HNRNPC reduces the expression of CELF2 via m6 A modification**

Next, we will further investigate HNRNPC's role in the m6 A modification of CELF2. Initially, we knocked down HNRNPC in KG-1 and OCI-AML-5 cell lines and verified the knockdown efficiency using RT-qPCR. We selected the most efficient sh-HNRNPC-1 for further experiments (Figure S7 A). We also overexpressed HNRNPC in human AML cells, KG-1 and OCI-AML-5, and confirmed the overexpression using RT-qPCR (Figure S7B). Following the knockdown of HNRNPC, there was a significant increase in the expression level of

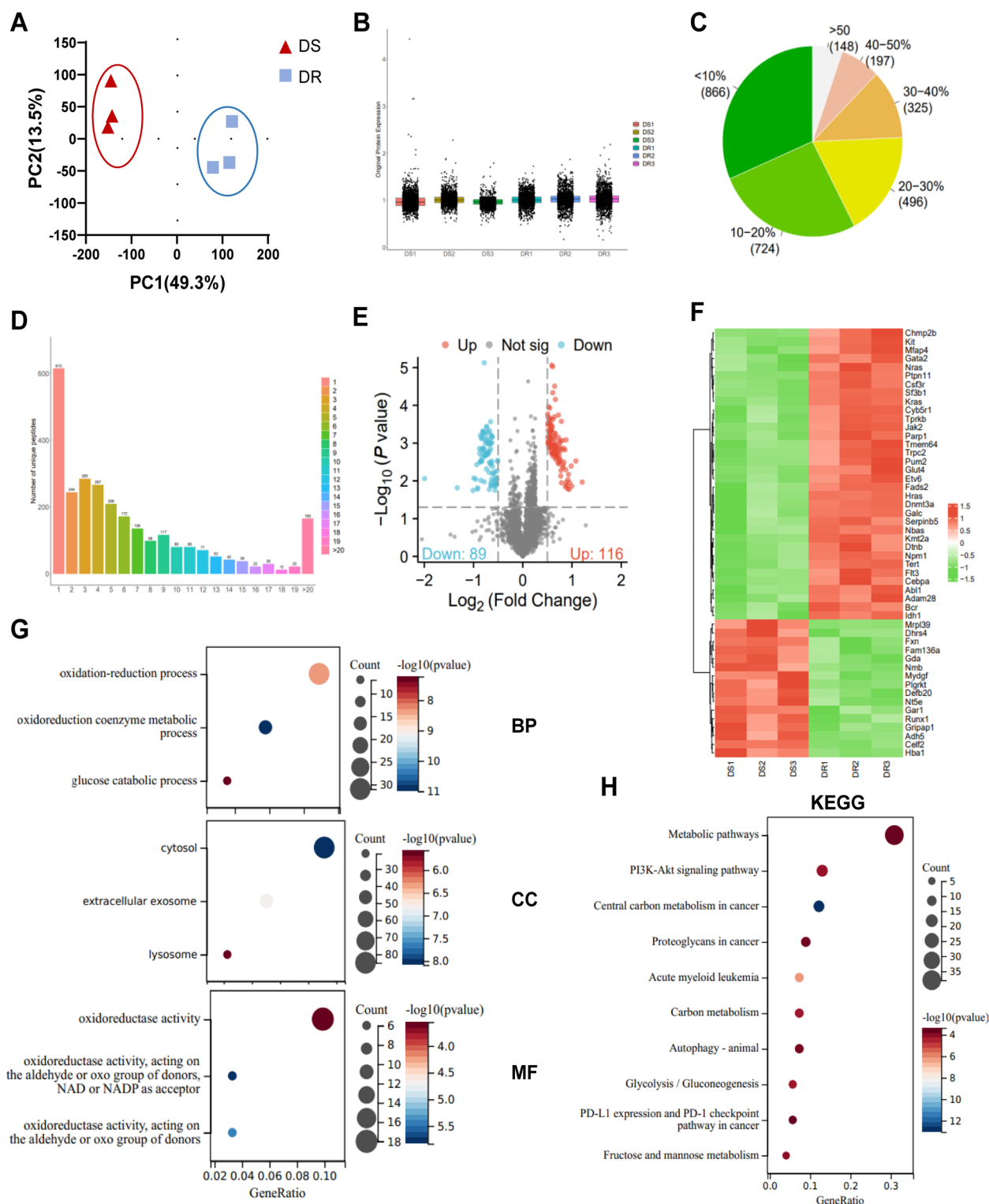


**Fig. 2** Molecular features of AML DR explored through proteomics. **A** Principal Component Analysis (PCA) showing the DS group (n = 3) and DR group (n = 3); **B** Box plots displaying reliable protein expression in the DS group (n = 3) and DR group (n = 3); **C** Distribution of sequence coverage of 2756 proteins; **D** Distribution of unique peptide counts for 2756 proteins; **E** Volcano plot showing significantly upregulated (red) and downregulated (blue) proteins, with no difference (gray) between the DS group (n = 3) and DR group (n = 3); **F** Heatmap of the top 50 significantly different proteins in the DS group (n = 3) and DR group (n = 3); **G, H** Functional enrichment analysis of significantly different proteins using GO **G** and KEGG **H**

CELF2, whereas the overexpression of HNRNPC led to a significant decrease in CELF2 expression (Fig. 4A).

To investigate the potential mechanism by which HNRNPC mediates selective splicing of CELF2, we first predicted the binding of HNRNPC to the chr10:11019141–11019176 region of CELF2 using the m6a2 target database (Fig. 4B; Figure S6B). Through MeRIP-qPCR, we found that the m6 A antibody significantly enriched CELF2 compared to the IgG antibody (Fig. 4C).

To measure the m6 A modification level, we performed m6 A dot blot analysis on AML cells. The results showed that knockdown of HNRNPC led to a significant decrease in m6 A modification in AML cells, while overexpression of HNRNPC resulted in a significant increase in m6 A modification (Fig. 4D).

Furthermore, to validate the relationship between m6 A modification and CELF2 mRNA expression, we constructed wild-type (WT) vectors containing the predicted m6 A sequence (WT-CELF2) and corresponding mutant (MUT) vectors (MUT-CELF2) (Fig. 4E). Subsequently, we generated respective luciferase reporter vectors and performed dual luciferase reporter gene experiments. The results revealed that overexpression of HNRNPC significantly reduced the luciferase activity of CELF2-WT, while there was no significant change in luciferase activity for MUT-CELF2. Knockdown of HNRNPC resulted in a significant increase in luciferase activity of CELF2-WT (Fig. 4F).

Half-life experiments showed that knocking down HNRNPC significantly prolonged the half-life of CELF2, whereas overexpression of HNRNPC significantly reduced the half-life of CELF2 (Fig. 4G).

In conclusion, HNRNPC can reduce the expression of CELF2 through m6 A modification.

### HNRNPC promotes AML cell proliferation and migration by regulating CELF2 expression through m6 A modification

Based on the bioinformatics analysis and in vitro cell mechanism verification mentioned above, it is indicated that HNRNPC may decrease the expression of CELF2 through m6 A modification, thereby regulating tumor cell proliferation and migration in AML cells. To further investigate whether HNRNPC decreases CELF2

expression through m6 A modification in AML cells, thus regulating tumor cell proliferation and migration, in this study, we first cultured KG-1 and OCI-AML-5 AML cell lines in a continuous 0.5  $\mu\text{g}/\text{mL}$  cytarabine solution for one month to induce DR (Figure S8 A). The cell viability assay confirmed that each drug-resistant clone exhibited significant resistance to Cytarabine compared to the parental cells (Figure S8B). Using RT-qPCR, we detected the expression levels of HNRNPC in the established drug-resistant cell lines, and the results showed a significant increase in the expression levels of HNRNPC in drug-resistant AML cells, while CELF2 expression was significantly decreased (Figure S8 C).

We knocked down HNRNPC or CELF2 in drug-resistant AML cells, and the results showed that down-regulating HNRNPC decreased its expression while increasing CELF2 expression. Further knockdown of CELF2 reduced its expression (Figure S7 C). Overexpressing HNRNPC or CELF2 in non-drug-resistant AML cells, on the other hand, showed increased HNRNPC expression and decreased CELF2 expression. Re-introducing CELF2 after overexpression resulted in restored expression levels (Figure S7D).

We used CCK-8 assays to verify the proliferation rates of cells in different treatment groups. The results showed that the proliferation capacity of the drug-resistant cells was significantly reduced when HNRNPC was knocked down. However, the subsequent knockdown of CELF2 significantly increased the proliferation capacity. Conversely, overexpressing HNRNPC in non-drug-resistant cells significantly increased their proliferation capacity. Additionally, overexpressing CELF2 resulted in a significant decrease in cell proliferation rate (Fig. 5A). Furthermore, we performed IC50 tests to measure the DR of each cell group to Cytarabine. The results showed that knocking down HNRNPC significantly reduced DR, while further knockdown of CELF2 increased DR. Conversely, overexpression of HNRNPC had the opposite effect, and overexpression of CELF2 resulted in reduced DR (Figure S8D).

Transwell assays were conducted to assess cell migration ability. The results showed that the knockdown of HNRNPC significantly reduced the migration capacity of

(See figure on next page.)

**Fig. 3** Molecular mechanisms of AML DR analyzed through integrated scRNA-seq and proteomics. **A** Volcano plot comparing differential gene expression of AML cell clusters in the scRNA-seq dataset between the DS group ( $n = 3$ ) and DR group ( $n = 3$ ), with red indicating significantly upregulated genes, blue indicating significantly downregulated genes and gray indicating non-significant genes; **B** Venn diagram showing the overlap of differentially expressed genes and differentially expressed proteins; **C** PPI network of 18 intersected genes predicted using the String website; **D** Violin plots showing the expression of CELF2, HNRNPC, and FUS in AML cells in the scRNA-seq dataset; **E** Box plots illustrating the expression of CELF2, HNRNPC, and FUS in the proteomics dataset; **F** Pseudotime analysis of the DR group; **G** Violin plots displaying the distribution of CELF2 and HNRNPC expression levels across cell types; the x-axis represents cell types, and the y-axis represents gene expression levels, with differences between two groups analyzed using t-tests. \* indicates  $p < 0.05$

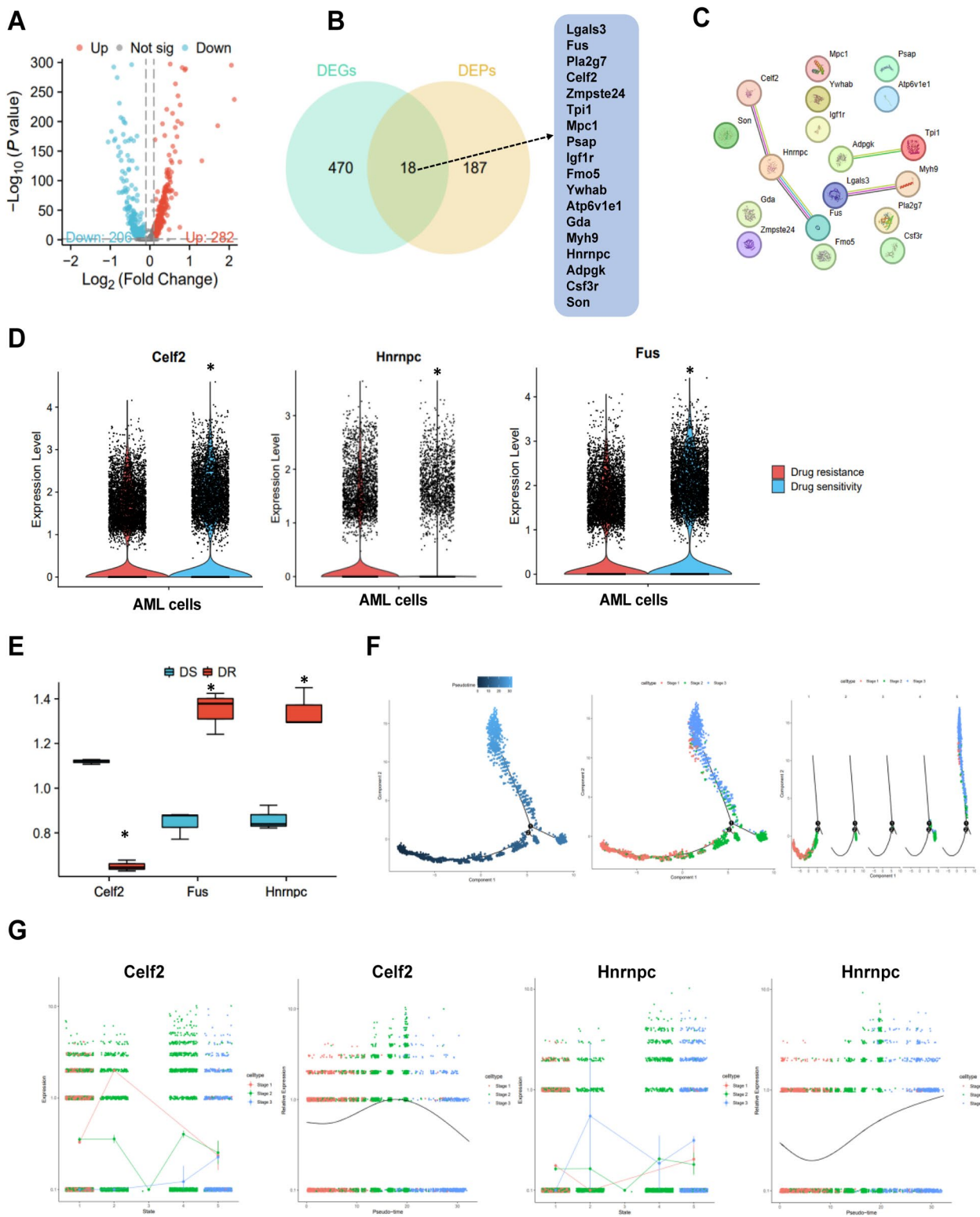


**Fig. 3** (See legend on previous page.)

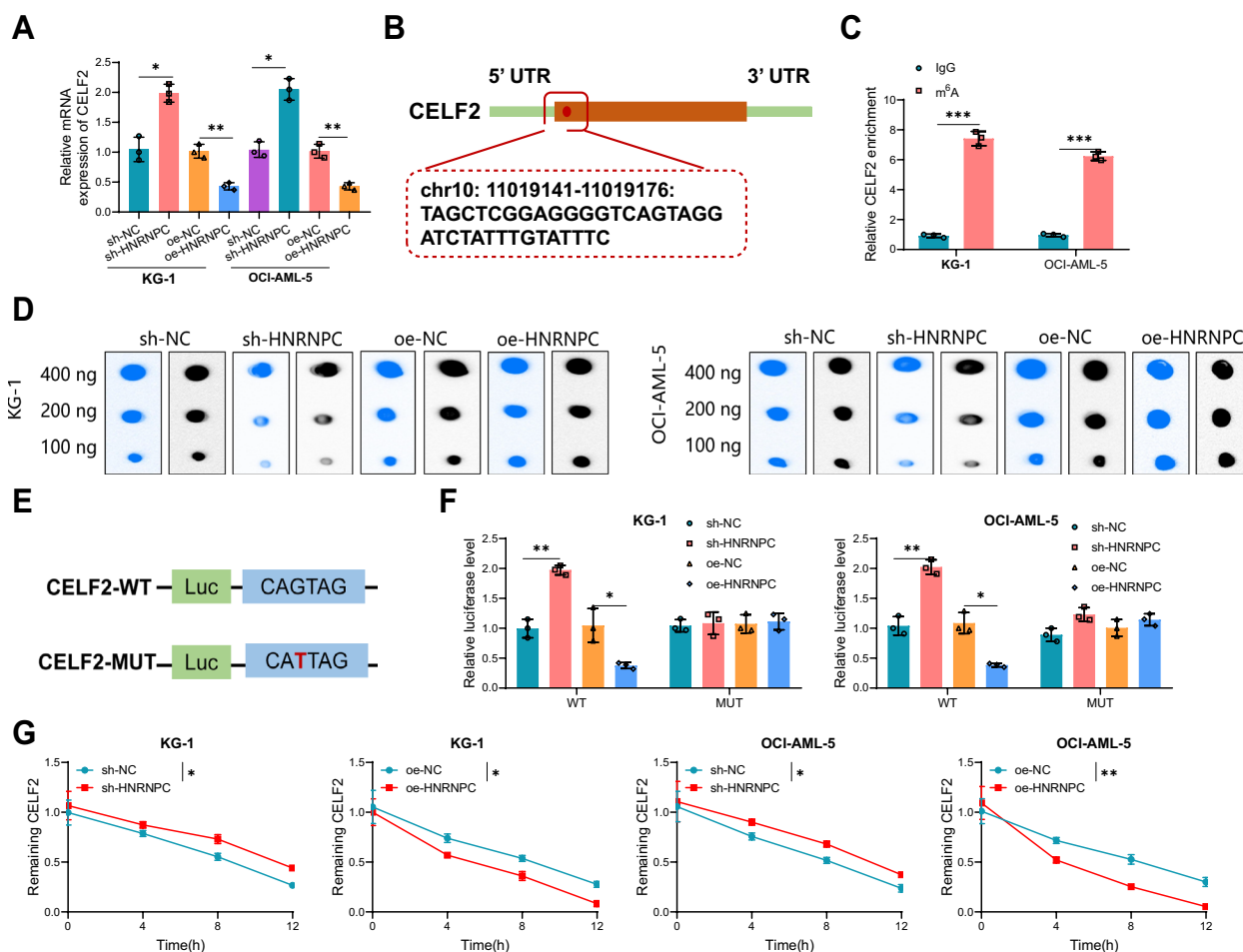


**Fig. 4** Investigating the m6 A modification of CELF2 by HNRNPC. **A** RT-qPCR analysis of the effect of HNRNPC knockdown or overexpression on CELF2 expression levels; **B** Schematic diagram of the predicted binding region between HNRNPC and CELF2 using the m6a2 target database; **C** meRIP experiment to detect m6 A modification of CELF2; **D** m6 A levels in AML cells measured by m6 A dot blots; **E** Schematic diagram of CELF2 binding region mutation sites; **F** Dual-luciferase reporter gene assay to measure luciferase activity in cells from different treatment groups; **G** Assessment of RNA(K) degradation rates in cells treated with streptomycin D in control, HNRNPC knockdown, or overexpressing cells. All cell experiments were repeated three times, and results are presented as mean ± standard deviation, with differences between two groups analyzed using t-tests. \* indicates  $p < 0.05$ , \*\* indicates  $p < 0.01$ , \*\*\* indicates  $p < 0.001$

drug-resistant cells, while the simultaneous knockdown of CELF2 significantly increased the migration of KG-1/DR cells. Overexpression of HNRNPC significantly increased the migration capacity of OCI-AML- 5/DR cells, while re-introducing CELF2 significantly decreased cell migration (Fig. 5B).

Flow cytometry was used to study cell apoptosis rates. The experimental results indicated that the knockdown of HNRNPC increased the apoptosis of drug-resistant cells, which could be reversed by sh-CELF2. Overexpression of HNRNPC significantly reduced cell apoptosis, but subsequent overexpression of CELF2 resulted in a significant increase in apoptosis rates (Fig. 5C).

To better approximate the in vivo environment, we constructed 3D cancer spheroids of AML cell lines. After 48 h of transfection, invasion of the spheroids was observed, and the results showed that the invasion ability of drug-resistant spheroids was higher than non-drug-resistant spheroids. The invasive characteristics of drug-resistant sh-HNRNPC spheroids significantly decreased, but the simultaneous knockdown of CELF2 significantly increased invasion. Compared to the control group, the non-drug-resistant oe-HNRNPC group showed a significant increase in invasion ability; however, invasion ability significantly decreased after overexpression of CELF2 (Fig. 5D).

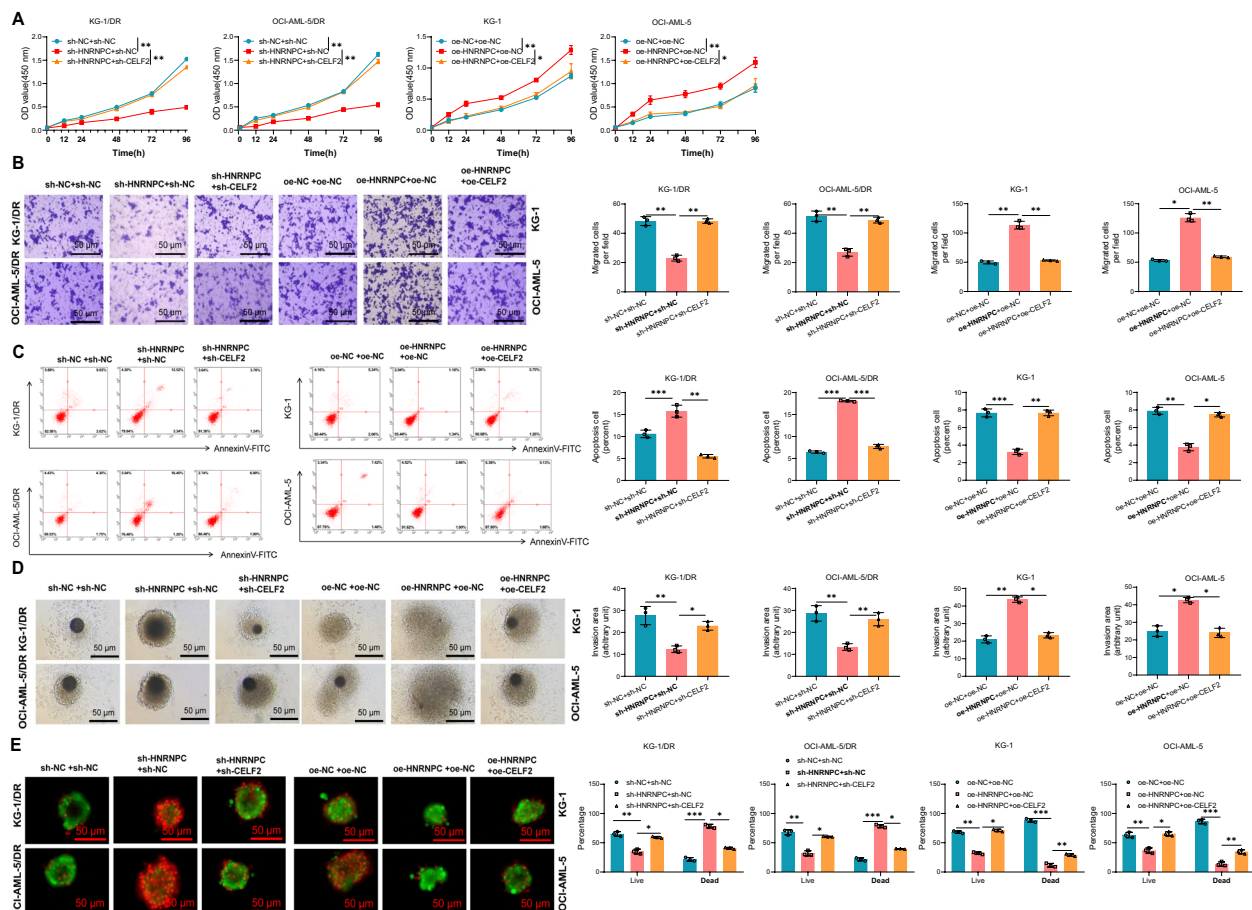


**Fig. 5** Role of HNRNPC in AML cell DR mechanisms. **A** CCK8 assay to detect tumor cell proliferation at different time points; **B** Transwell experiment to evaluate the migration ability of AML cells, bar = 10  $\mu$ m, the right panel shows the statistical graph; **C** Flow cytometry analysis of tumor cell apoptosis, apoptotic cells are marked by red squares, the right panel shows the statistical graph; **D** Cell culture images captured in bright field mode under an inverted microscope, the invaded region is outlined by a white dashed line, bar = 2  $\mu$ m, right panel shows the statistical graph of the invaded region; **E** Confocal microscopy images of viability determination in cancer spheroids, live cells stained with calcein-AM (green), dead cells stained with EthD-1 (red), bar = 50  $\mu$ m, right panel shows the statistical graph of live/dead cells in cancer spheroids. All cell experiments were repeated three times, and the values are presented as mean  $\pm$  standard deviation. Asterisks denote statistical significance: \* $p$  < 0.05, \*\* $p$  < 0.01, \*\*\* $p$  < 0.001

We stained viable cells with calcium green-1 AM and dead cells with EthD-1. Microscopic observation revealed that the majority of AML cells in the HNRNPC knockdown group underwent cell death, while simultaneous knockdown of CELF2 promoted cell survival. Most AML cells in the HNRNPC overexpression group remained alive, but cell death increased after overexpression of CELF2 (Fig. 5E).

Taken together, these experimental results demonstrate that HNRNPC promotes AML cell proliferation and migration by suppressing CELF2 expression through m6A modification.

### Metabolomics analysis reveals glycolytic pathway as a key metabolic pathway in AML DR mechanism

The progression and development of tumors require cancer cells to undergo metabolic reprogramming [29]. Alterations in the energy metabolism of cancer cells can satisfy the need for rapid proliferation and adaptation to the tumor microenvironment [30]. Energy metabolism reprogramming is one of the hallmarks of cancer, with abnormal glucose metabolism and high dependence on glucose being typical features of tumor metabolism [31].

To identify metabolites influencing AML DR, we collected six groups of KG-1/DR cells and six groups of

KG-1 cells and performed a non-targeted metabolomic analysis using liquid chromatography-mass spectrometry (LC-MS). Multivariate analysis using principal component analysis (PCA) and orthogonal partial least squares-discriminant analysis (OPLS-DA) models was applied to visualize the changes in cell metabolism. Our experimental results demonstrated a clear separation of metabolite profiles between the resistant and non-resistant groups (Fig. 6A, B).

Differential metabolites were selected through multivariate analysis and t-test. A total of 35 differential metabolites were identified, with 18 upregulated and 17 downregulated (Fig. 6C). Subsequently, hierarchical clustering and Euclidean distance analysis were performed to cluster the differential metabolites, visualized through a hierarchical cluster heatmap (Fig. 6D).

Enrichment pathway network analysis revealed significant involvement of metabolites in gluconeogenesis/glycolysis metabolism (Fig. 6E, F). Functional enrichment analysis showed that, in the SMPDB database, differential metabolites were mainly enriched in pathways such as Gluconeogenesis, Glycolysis, and the Warburg Effect (Fig. 6G). In the KEGG database analysis, differential metabolites were mainly enriched in pathways such as Glycolysis/Gluconeogenesis, Pyruvate metabolism, and Inositol phosphate metabolism (Fig. 6H).

In our KEGG enrichment analysis of differentially expressed proteins, we also observed significant enrichment in the Glycolysis/Gluconeogenesis pathway. Therefore, it is speculated that the glycolytic metabolism pathway is involved in the formation of AML DR mechanism.

#### HNRNPC Reprograms cellular glucose metabolism by inhibiting CELF2 expression

Under conditions of sufficient oxygen, cancer cells often exhibit an abnormal glucose metabolism pattern, whereby they preferentially convert glucose into lactate through glycolysis, even in aerobic conditions. This particular metabolic pathway is known as aerobic glycolysis or the "Warburg effect"[32]. Furthermore, metabolic profiling analysis, particularly using the SMPDB database, has shown significant enrichment of the Warburg effect

pathway. Based on these observations, we hypothesized that the HNRNPC/CELF2 signaling pathway may contribute to AML DR through the promotion of glycolysis.

To validate this hypothesis, we first examined the expression of glycolysis-related genes, such as GLUT1, HK2, LDHA, and PDK1, in AML cells using RT-qPCR and Western blot techniques [33]. The experimental results demonstrated that knocking down HNRNPC significantly reduced the expression levels of these genes, whereas simultaneous knockdown of CELF2 increased their expression levels. Conversely, overexpression of HNRNPC significantly increased the expression of these glycolysis-related genes, which could be reversed by overexpressing CELF2 (Fig. 7A, B).

Mitochondria are essential organelles involved in glycolysis [34]. We utilized JC-1 dye, a lipophilic cationic dye specifically used to measure mitochondrial membrane potential ( $\Delta\psi_m$ ), to determine the mitochondrial membrane potential in AML cells. The experimental results indicated that knocking down HNRNPC led to a significant decrease in  $\Delta\psi_m$ , while overexpression of HNRNPC resulted in a significant increase. Additionally, sh-CELF2 or oe-CELF2 could respectively reverse these effects (Fig. 7C).

We also assessed the levels of total intracellular reactive oxygen species (ROS) and mitochondrial ROS. ROS staining results revealed a significant decrease in ROS in the sh-HNRNPC cell group, whereas ROS levels significantly increased in the oe-HNRNPC cell group (Fig. 7D). These data suggest that HNRNPC reprograms the energy metabolism of AML cells.

Moreover, we evaluated mitochondrial quality using the MitoTracker staining technique. The data showed a significant increase in mitochondrial quality upon HNRNPC knockdown, whereas simultaneous knockdown of CELF2 resulted in a significant decrease in mitochondrial quality. Conversely, overexpression of HNRNPC led to a decrease in mitochondrial quality, which was significantly increased upon CELF2 overexpression (Fig. 7E).

Furthermore, we measured the oxygen consumption rate (OCR) and extracellular acidification rate (ECAR) of AML cells in an activated state using the Seahorse device,

(See figure on next page.)

**Fig. 6** Metabolomic Analysis of drug-resistant and non-resistant cell groups. **A, B** Principal Component Analysis (PCA) plot **A** and Partial Least Squares Discriminant Analysis (PLS-DA) plot **B** of the drug-resistant group (n = 6) and non-resistant group (n = 6); **C** Volcano plot showing differentially expressed metabolites, red represents significantly upregulated metabolites, blue represents significantly downregulated metabolites, gray represents non-significant differential metabolites; **D** Heatmap visualization of significantly different metabolites; **E, F** Participation of differentially expressed metabolites in the glycolysis/gluconeogenesis pathway in enrichment pathway analysis, red indicates metabolites involved in the enrichment items; **G, H** Functional enrichment analysis of all differentially expressed metabolites using SMPDB **G** and KEGG **H** databases, P values in the metabolic pathways indicate the importance of metabolite enrichment

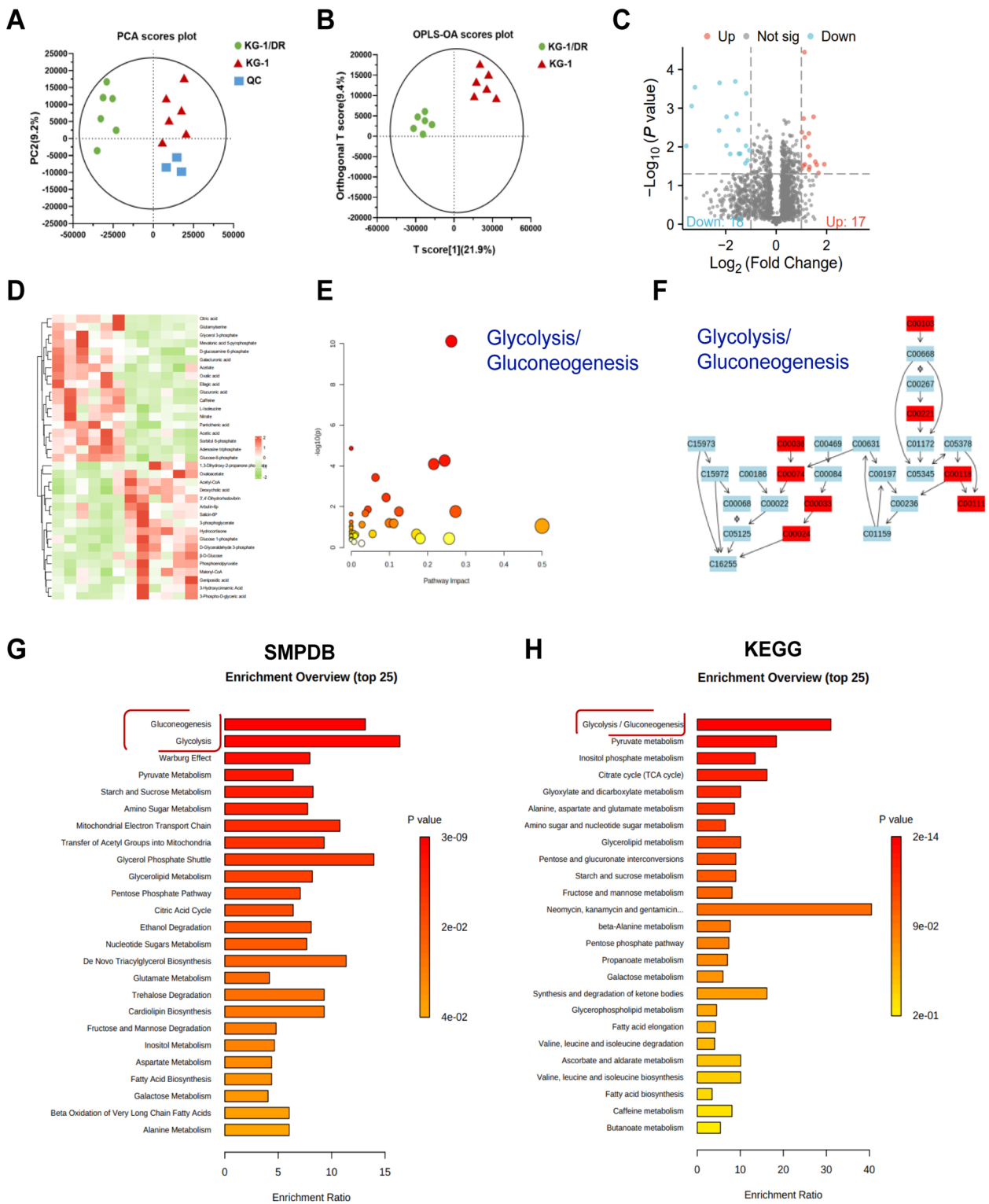


Fig. 6 (See legend on previous page.)

which reflects oxidative phosphorylation (OXPHOS) and aerobic glycolysis, respectively. The results demonstrated that knocking down HNRNPC decreased glycolysis in cells, which was reversed by sh-CELF2. Conversely, overexpression of HNRNPC increased glycolysis, but this effect was significantly reduced upon on-CELF2 expression (Fig. 7F–G).

These experimental findings indicate that in AML cells, HNRNPC reprograms cellular glucose metabolism by suppressing CELF2 expression. This reprogramming manifests through increased expression of glycolysis-related genes, modulation of mitochondrial function, and alterations in cellular energy metabolism.

#### HNRNPC promotes AML cell metabolic reprogramming by suppressing CELF2

In our *in vitro* experiments, we discovered that HNRNPC promotes metabolic reprogramming in AML cells by inhibiting CELF2, potentially accelerating AML progression. To validate this finding further, KG-1 and KG-1/DR cell lines (after transfection) were transplanted subcutaneously into nude mice to establish a tumor model. After 15 days of transplantation, Cytarabine treatment was initiated (dose: 3 mg/kg/d) (Fig. 8A).

Before drug treatment, the expression levels of HNRNPC and CELF2 were measured in tumor tissues of the resistant group and non-resistant group using RT-qPCR and Western blot techniques. The results showed a significant increase in HNRNPC expression and a significant decrease in CELF2 expression in group G3 compared to group G1. Furthermore, CELF2 expression was significantly increased in group G5 compared to group G3. Within the resistant group, HNRNPC expression was significantly reduced in groups G3/DR and G4/DR compared to groups G1/DR and G2/DR, while CELF2 expression was significantly increased. In group G5/DR, CELF2 expression was significantly lower than in group G3/DR (Fig. 8B, C).

Bioluminescence imaging was used to observe tumor luminescence images at 15, 25, and 30 days after tumor cell injection and tumor size was calculated. The results indicated that Cytarabine treatment alone had minimal therapeutic effect on the resistant mouse model.

However, knocking down HNRNPC in the resistant group reduced tumor formation, while knocking down CELF2 significantly increased tumor growth. In the non-resistant group, overexpression of HNRNPC counteracted the therapeutic effect of Cytarabine, whereas overexpression of CELF2 reversed this effect (Fig. 8D–F).

On day 30, tumor samples were analyzed (Fig. 8G), and the proliferative marker Ki67 in tumor tissues was studied using immunohistochemical techniques. The results showed that the knockdown of HNRNPC significantly decreased Ki67 expression in the resistant group, which was subsequently increased after sh-CELF2 treatment. In the non-resistant group, Cytarabine treatment alone reduced Ki67 expression, while overexpression of HNRNPC significantly increased Ki67 expression, which was counteracted by overexpression of CELF2.

These experimental results further confirm our hypothesis that HNRNPC accelerates AML progression by suppressing CELF2.

#### Discussion

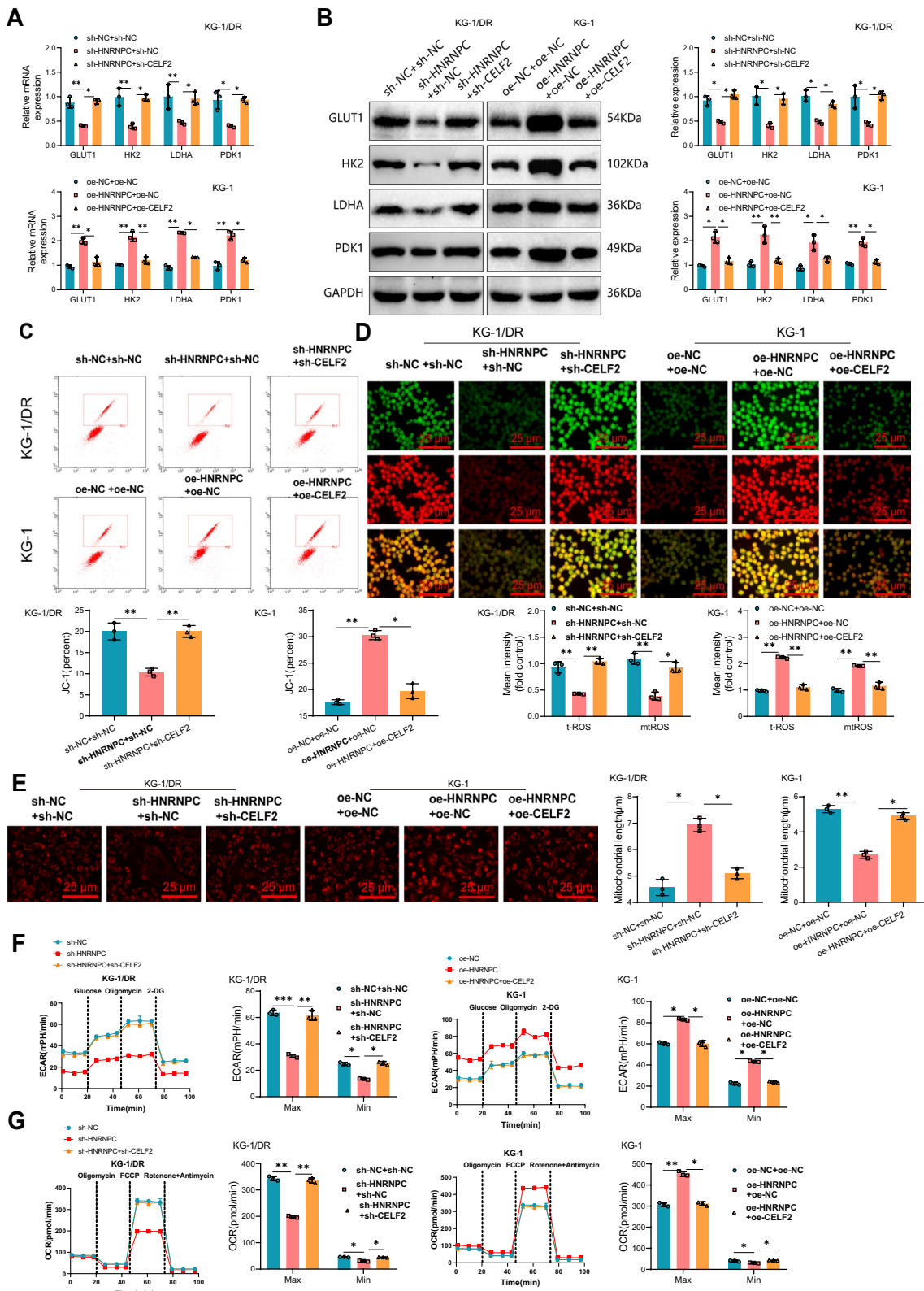
The aim of this study was to investigate the role of the HNRNPC/CELF2 signaling pathway in AML and its impact on tumor progression, metabolic reprogramming, and DR. AML, as a malignant tumor, still faces many challenges in its treatment [5, 7, 35]. It has been found that tumor cells can adapt to adverse environments by altering metabolic pathways, and glucose metabolism reprogramming plays a crucial role in this adaptive process [36–38].

In comparison with other studies, this research employed several omics analysis methods, including single-cell transcriptomics, iTRAQ labeling combined with mass spectrometry-based proteomics identification, to validate the roles of HNRNPC and CELF2 in various aspects of cell migration, proliferation, and invasion. These results enhance our understanding of the HNRNPC/CELF2 signaling pathway in AML and further elucidate its role in glucose metabolism reprogramming.

In this study, we found that HNRNPC influences the alternative splicing of CELF2 through m6A modification. We hypothesize that HNRNPC may act as an m6A reader, recognizing m6A modification sites on CELF2

(See figure on next page.)

**Fig. 7** Impact of HNRNPC/CELF2 signaling pathway on AML cell glucose metabolism. **A, B** Expression levels of GLUT1, HK2, LDHA, and PDK1 in AML cells detected by RT-qPCR **A** and Western blot **B**; **C** Measurement of JC-1 signals in cells using flow cytometry, calculation of the red/green signal ratio to determine mitochondrial potential; **D** Measurement and quantification of cellular ROS (green) and mtROS (red) in AML cells, statistical graph representation; **E** Quantification of mitochondrial morphology using MitoTracker staining (red), representation of statistical graph of mitochondrial length; **F, G** Minimum and maximum ECAR **F** and OCR **G** of AML cells. All cell experiments were repeated three times, and the values are presented as mean  $\pm$  standard deviation. Asterisks denote statistical significance, with differences between two groups analyzed using t-tests. \* indicates  $p < 0.05$ , \*\* indicates  $p < 0.01$



and ultimately regulating CELF2 expression [39], thereby modulating the growth and invasion ability of AML cells. This finding is consistent with other research, emphasizing the importance of the HNRNPC/CELF2 signaling pathway in tumor development [40–43]. By extensively studying the impact of the HNRNPC/CELF2 signaling pathway on the biological behavior of AML cells, we have laid the foundation for further understanding its mechanism of action.

Furthermore, this study revealed that HNRNPC significantly regulates the metabolic reprogramming of AML cells by suppressing CELF2 expression. Increased expression of HNRNPC and decreased expression of CELF2 in drug-resistant AML cells led to a significant increase in the expression levels of glycolysis-related genes, glucose consumption, lactate production, and mitochondrial dysfunction. These findings align with the discoveries of other studies, further validating the crucial role of glucose metabolism reprogramming in AML DR [44–47].

In conclusion, this study identified key genes, HNRNPC and CELF2, in AML cells through single-cell transcriptomics and proteomics identification. HNRNPC regulates CELF2 expression through m6 A modification, potentially playing a crucial role in AML DR (Fig. 9). The scientific and clinical value of this study lies in elucidating the importance of the HNRNPC/CELF2 signaling pathway in AML, as well as its involvement in glucose metabolism reprogramming and DR. Experimental results from cell and animal models reveal that HNRNPC-induced metabolic reprogramming of AML cells by suppressing CELF2 expression promotes DR and progression of AML. This finding offers new targets for AML treatment and helps improve existing therapeutic approaches, particularly in addressing DR. The research findings also provide a foundation for further development of treatment strategies based on these molecular targets.

Despite the consistent findings from both animal models and in vitro cell experiments, this study has certain limitations. First, the sample size for the DR ( $n = 6$ ) and DS ( $n = 10$ ) groups is relatively small. While the results provide valuable insights, additional biological replicates would strengthen statistical power and reproducibility. Second, although this study reveals the HNRNPC-CELF2

regulatory mechanism in vitro, its in vivo function remains to be fully validated, which is crucial for establishing clinical relevance. Third, while our study explores the HNRNPC-CELF2 axis in AML, the broader molecular mechanisms underlying AML drug resistance and disease progression are not yet fully understood, indicating the need for further investigation. Additionally, this study does not cover all potential factors influencing AML drug resistance and progression, suggesting that other unknown mechanisms may also be involved.

For future research, expanding the sample size and incorporating clinical correlation data from AML patients will enhance the clinical applicability of these findings. Further in vivo studies validating the HNRNPC-CELF2 axis would provide stronger evidence supporting its potential as a therapeutic target. Additionally, investigating the interaction between this pathway and other molecular signaling pathways or therapeutic approaches may lead to more effective AML treatment strategies. Future studies should also explore the role of the HNRNPC-CELF2 axis in other leukemia subtypes and malignancies, broadening its potential application in cancer research and treatment. In conclusion, this study provides critical insights into AML drug resistance mechanisms and highlights a potential therapeutic target, offering guidance for future research and clinical treatment strategies.

## Materials and methods

### Cell culture

The AML cell lines C1498 (M5 - 1301, Sibas BioTech Co., Ltd., Guangzhou, China), KG- 1 (SNL- 180, Sunchon Bio, Wuhan, China), and OCI-AML- 5 (Chuanqiu Bio, Shanghai, China) were cultured in DMEM media (11965092, Gibco, USA) supplemented with 1% penicillin–streptomycin (10378016, Invitrogen, USA) and 10% fetal bovine serum (FBS, Gibco, 10100147, Invitrogen, USA). The cells were incubated at 37 °C and 5% CO<sub>2</sub> in a cell culture incubator. The growth media were changed every 3 days [48].

To induce DR, the KG- 1 and OCI-AML- 5 cell lines were exposed to a concentration of 0.5 µg/mL cytarabine

(See figure on next page.)

**Fig. 8** Validation of the role of HNRNPC/CELF2 signaling pathway in AML tumor progression. **A** Illustration of tumor formation in nude mice; **B, C** Expression levels of HNRNPC and CELF2 in tumor tissue detected by RT-qPCR (**B**) and Western blot (**C**); **D** In vivo imaging of mice using near-infrared imaging technique after subcutaneous injection of AML cells, the right panel semi-quantitatively displays the signal of AML cells in the tumor; **E** Relative changes in tumor volume for each group of mice; **F** Illustration of subcutaneous tumors in each group of mice; **G** Expression levels of Ki67 in tumor tissue detected by immunohistochemistry, representation of statistical graph of positive cells. Each group of mice had 6 individuals, and the values are presented as mean ± standard deviation. Asterisks denote statistical significance, with differences between two groups analyzed using t-tests. \* indicates  $p < 0.05$ , \*\* indicates  $p < 0.01$ , \*\*\* indicates  $p < 0.001$

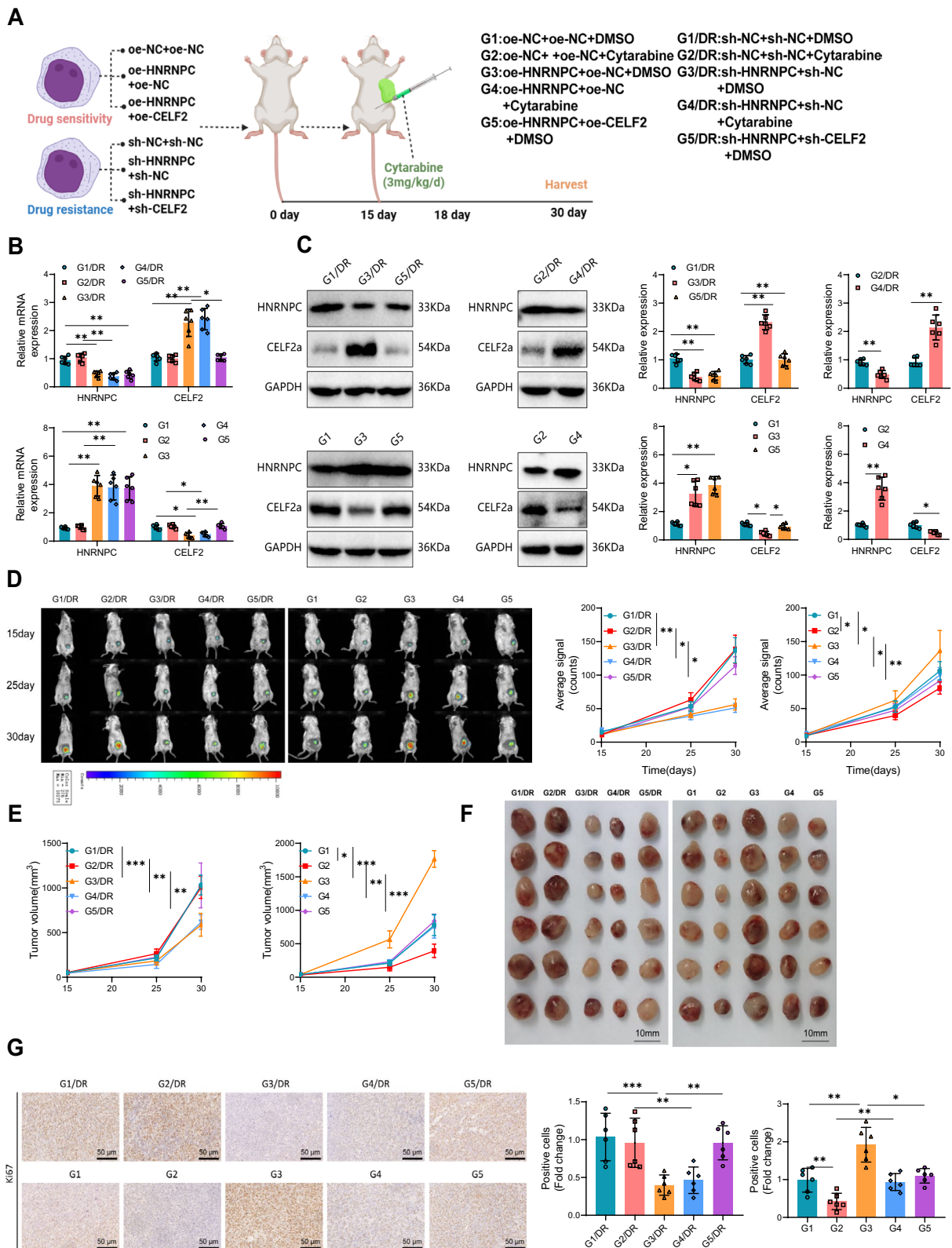


**Fig. 8** (See legend on previous page.)

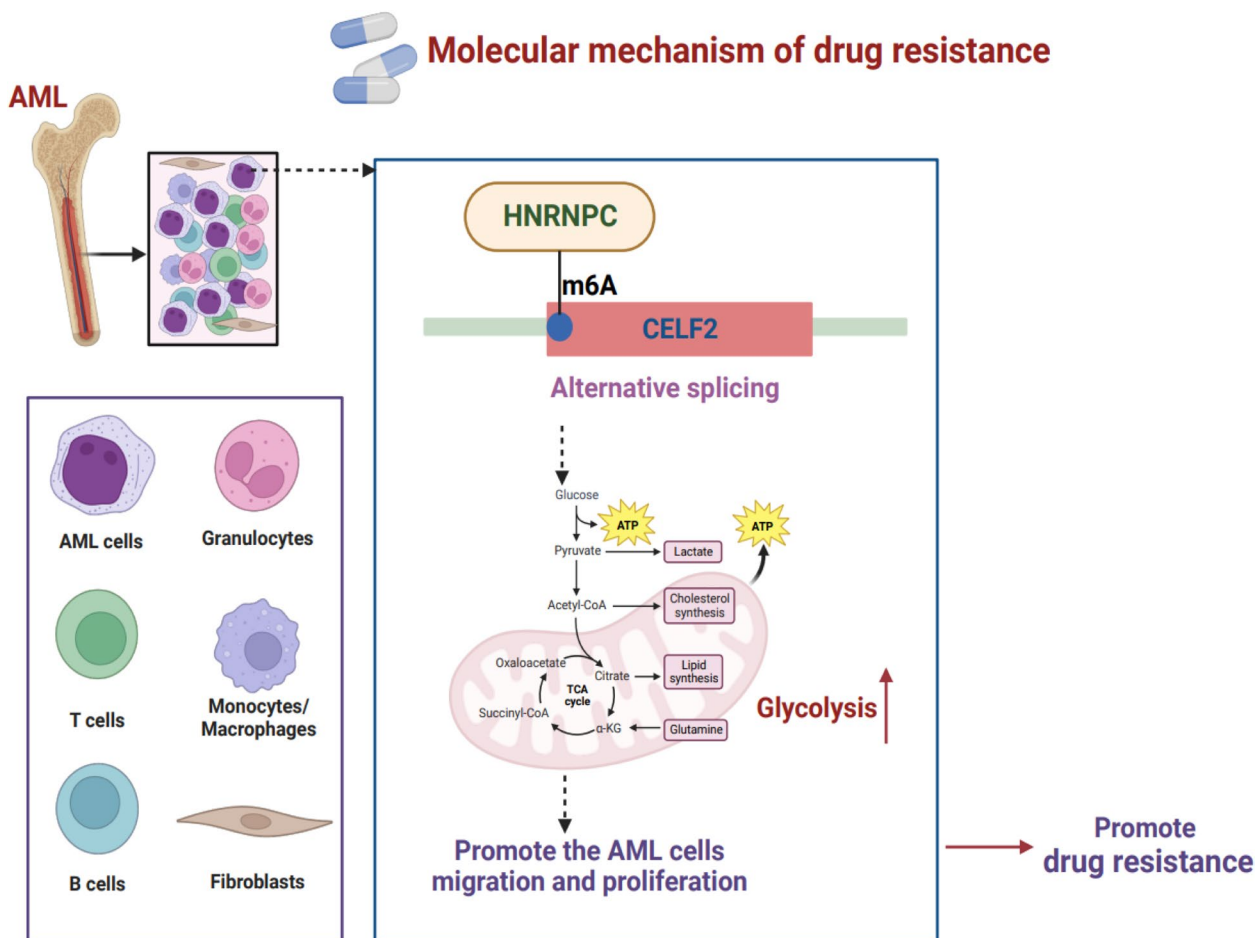


**Fig. 9** Molecular mechanism diagram illustrating how HNRNPC affects CELF2 selective splicing by m6 A methylation, promoting AML glycolytic reprogramming-induced DR

(147 -94- 4, Shanghai Nuojie Chemical Technology Co., Ltd., Shanghai, China) for one month [49].

**Construction of AML drug-resistant mouse model**

Female C57BL/6 J mice at 4 weeks old and female BALB/c-nu mice at 6 weeks old were purchased from our Animal Experimental Center. All animal experiments were conducted following our institution’s “Guidelines for the Care and Use of Laboratory Animals”.

The C1498 cell line (M5 -1301, Sibas BioTech Co., Ltd., Guangzhou, China) was electroporated with pLVX-mCMV-ZsGreen1-Puro (HG-VMH1097, IbiVet Biotechnology, Changsha, China) to produce a stable fluorescent protein-expressing C1498 sub-clone [50]. Firstly, we administered sublethal whole-body irradiation (450 cGy) to the 4-week-old female C57BL/6 J mice to suppress their bone marrow hematopoietic function. Then, we established the AML mouse model by injecting 10<sup>5</sup> C1498 AML cells expressing ZsGreen1 fluorescent protein via tail vein injection. Starting from day 14, each

mouse was treated with Cytarabine (3 mg/kg/d) by intraperitoneal injection to treat AML. The mice were monitored for survival or euthanized whenever they showed signs of distress (e.g., isolated in a cage corner, slow movement, and dull fur). After 35 days of modeling, mice were euthanized by cervical dislocation under deep anesthesia using isoflurane (R510-22 -10, Revoth, Shenzhen, China) [22].

**Hematological analysis**

Peripheral blood samples were collected from the mice and analyzed for red blood cell count (RBC), white blood cell count (WBC), and platelet count (PLT) using a Vitos5.1 FS automated biochemical analyzer (Ortho Clinical Diagnostics, USA) [51].

**Flow cytometry**

Bone marrow tissue cells were collected and sorted using anti-CD11b (BDB561690, BD Bioscience, USA), anti-CD41a (11-0411- 82, Thermo Fisher, USA), anti-Ter119

(ab93586, Abcam, UK), anti-PD-L1 (569074, BD Bioscience, USA), and anti-CTLA-4 (12-1529-42, Thermo Fisher, USA) antibodies. After thorough mixing, the cells were incubated at 4 °C in the dark for 30 min. Then, 2 mL of PBS solution (P4417, Sigma-Aldrich, USA) was added, and the mixture was centrifuged at 4 °C, 1500 ×g for 10 min. After discarding the supernatant, the cells were fixed with a 2% paraformaldehyde (30525-89-4, Sigma-Aldrich, USA)/PBS solution, placed at 4 °C in the dark, and analyzed using a FACS Aria II flow cytometer (BD Bioscience, USA) within 24 h [52].

Cell apoptosis was assessed using the Annexin V-FITC apoptosis detection kit (APOAF-20 TST, Sigma-Aldrich, USA) via flow cytometry according to the manufacturer's instructions. The cells were plated at a density of  $4 \times 10^5$  cells per well in a 6-well plate and allowed to attach overnight. Subsequently, the cells were treated with different concentrations of Cytarabine (0.125, 0.25, 0.5 µg/mL) for 48 h. After drug treatment, the cells were incubated with 200 µL binding buffer, stained with Annexin V-FITC in the dark for 20 min, and then analyzed using a FACS Aria II flow cytometer [53]. Cells in the upper right quadrant with the Annexin V+ PI+ phenotype represented late apoptosis cells, while cells with the Annexin V+ PI- phenotype in the lower right quadrant represented early apoptosis cells. Cells in the upper left quadrant with the Annexin V- PI+ phenotype represented necrotic cells, and cells in the lower left quadrant with the Annexin V- PI- phenotype represented viable cells [54].

JC-1 staining: AML cells were cultured in high glucose RPMI-1640 medium (R8758, Sigma-Aldrich, USA, 4.5 g/L glucose) and analyzed using the JC-1 mitochondrial membrane potential assay kit (C2006, Beyotime, Shanghai, China) via flow cytometry after 24 h of culture. The ratio of JC-1 red to JC-1 green was used to indicate the  $\Delta\psi_m$  of the cells [55].

### Immunofluorescence staining

Cells or tissues were washed with cold PBS and fixed with 4% paraformaldehyde (P885233, Macklin, USA) for 15–30 min. Subsequently, they were treated with 0.1% Triton (L885651, Macklin, USA) for 15 min. After two washes with PBS, cells or tissues were incubated with PBS containing 15% FBS at 5 °C overnight. They were then stained with antibodies against CD11b (MA1-80091, Thermo Fisher, USA; 1:50) for rats, CD41a (ab134131, Abcam, UK; 1:100) for rabbits, Ter119 (14-5921-82, Thermo Fisher, USA; 1:100) for rats, PD-L1 (14-5983-82, Thermo Fisher, USA; 1:100) for mice, or CTLA-4 (711564, Thermo Fisher, USA; 1:100) overnight at 4 °C. After washing three times with TBST (1% Tween-20 in TBS), the cells were incubated with secondary antibodies: goat anti-rabbit Alexa Fluor® 647 (A-21245, Thermo

Fisher, USA), goat anti-rat Alexa Fluor® 647 (A-21247, Thermo Fisher, USA), goat anti-mouse Alexa Fluor Plus 488 (A32723, Thermo Fisher, USA), or monkey anti-rabbit Alexa Fluor® 555 (A-31572, Thermo Fisher, USA) for 2 h at room temperature. Subsequently, the cells were counterstained with DAPI (D1306, Thermo Fisher, USA) and observed under a fluorescence microscope (Zeiss Observer Z1, Germany). Target regions were selected in the images for fluorescence intensity measurement. Image processing and quantification were performed using ImageJ to determine the number of positive cells [56].

### scRNA-seq

The bone marrow tissues of AML mice were collected and processed into single-cell suspension using trypsin (9002-07-7, Sigma-Aldrich, USA). Individual cells were captured using the C1 single-cell auto-preparation system (Fluidigm, Inc., South San Francisco, CA, USA). After cell capture, the cells were lysed within the chip to release mRNA, which was then reverse-transcribed into cDNA. The lysed and reverse-transcribed cDNA was pre-amplified in a microfluidic chip for subsequent sequencing. The amplified cDNA was used for library construction and subjected to single-cell sequencing on the HiSeq 4000 Illumina platform (parameters: paired-end reads, read length  $2 \times 75$  bp, approximately 20,000 reads per cell) [57].

The data were analyzed using the "Seurat" package in R software. Quality control was performed using the criteria of  $200 < nFeature\_RNA < 5000$  percent.mt  $< 20$ , followed by the selection of the top 2000 genes with high expression variability [58].

Data analysis was performed using the "Seurat" package in R. For quality control, cells were selected based on the criteria  $200 < nFeature\_RNA < 5000$  and percent.mt  $< 20$ , ensuring that low-quality or dead cells (such as those with high mitochondrial gene expression, e.g., over 20%) were excluded from the analysis [58]. The data was then normalized using the "NormalizeData" function in the Seurat package with log-normalization, where gene expression data for each cell was normalized according to the total count and log-transformed. The parameters set were: normalization.method = 'LogNormalize', scale.factor = 10000. After normalization, the top 2000 highly variable genes were selected using the "FindVariableFeatures" function to ensure high-quality input for downstream analyses [58].

To reduce the dimensionality of the scRNA-Seq dataset, principal component analysis (PCA) was performed on the top 2000 highly variable genes using the "RunPCA" function in Seurat. The first 20 principal components were selected for downstream analysis using the

Elbowplot function. Cell subpopulations were identified using the "FindClusters" function with the default resolution ( $res = 1$ ), ensuring that the clustering was reasonable for distinguishing different cell types. Nonlinear dimensionality reduction was performed using t-SNE, with parameters set to "dims = 1:20" to ensure accurate dimensionality reduction. Marker genes for various cell subpopulations were identified using Seurat, and cells were annotated using the "Singel R" package [59].

Cell communication analysis was performed using the "CellChat" package in R, which inferred ligand-receptor interactions based on default parameters. Cell trajectory analysis was performed using the "Monocle2" package.

DEGs in the scRNA-Seq dataset were identified using the "Limma" package in R, with criteria of  $|\logFC| > 0.5$  and  $p < 0.05$ , followed by multiple comparison correction (Benjamini-Hochberg) [60].

The "inferCNV" package in R was used to assess copy number variation (CNV) in individual cells. This tool infers CNV instability in tumor scRNA-Seq data by comparing gene expression levels between normal and malignant cells, using granulocytes, fibroblasts, T cells, endothelial cells, and B cells as reference populations [61].

Gene ontology (GO) functional and Kyoto Encyclopedia of Genes and Genomes (KEGG) pathway enrichment analyses of co-expressed genes were performed using the "clusterProfiler" package in R, with a default p-value threshold ( $p < 0.05$ ) and visualization using the ggplot2 package [62].

#### iTRAQ labeling combined with mass spectrometry analysis

Mouse bone marrow tissues from the drug-resistant and non-resistant groups were collected. Protein extraction was performed by adding an appropriate amount of SDT lysis buffer (ED- 8452, ECOTOP, Guangzhou, China), followed by protein quantification using the BCA method (23227, Thermo Fisher, USA).

For each sample, 30  $\mu$ L of the protein solution was taken and subjected to protein digestion into peptides using the Filter-Assisted Sample Preparation (FASP) method. The peptides were then desalted using a C18 Cartridge (WAT051910, Waters, USA), concentrated by vacuum centrifugation, and resuspended in 40  $\mu$ L of the dissolution buffer (GS1422, Beijing Bioautotec Co., Ltd., Beijing, China). The resuspended peptides were measured at 280 nm using ultraviolet light. Subsequently, 100  $\mu$ g of peptides from each sample were labeled according to the instructions of the iTRAQ labeling kit (4352135, Sigma Aldrich, USA).

The iTRAQ-labeled peptides were fractionated using an AKTA Purifier 100 (GE, Sweden) with Strong Cation

Exchange (SCX) chromatography. Peptides were reconstituted, acidified, and separated using Solution A (10 mM KH<sub>2</sub>PO<sub>4</sub> in 25% acetonitrile, pH 3.0) and Solution B (500 mM KCl, 10 mM KH<sub>2</sub>PO<sub>4</sub> in 25% acetonitrile, pH 3.0). After freeze-drying, the peptides were desalted using a C18 Cartridge.

Each sample was separated using the Easy nLC system (Alliance HPLC, Waters, USA) with a nanoflow rate. Solution A was 0.1% formic acid in water, while Solution B was 0.1% formic acid in acetonitrile (acetonitrile concentration of 84%). The chromatography column was equilibrated with 95% Solution A, and the samples were loaded onto the trapping column (nanofiber C18, Thermo Fisher, USA) via an autosampler. Separation was performed using an analytical column (C18-A2, Thermo Fisher, USA) at a flow rate of 300 nL/min. After chromatographic separation, the samples were analyzed using a Q-Exactive mass spectrometer (Q Exactive™ Orbitrap, Thermo Fisher, USA) [63].

#### Differential expression of proteins (DEPs)

DEPs was analyzed using iTRAQ mass spectrometry data and statistical methods. Specifically, t-tests (Student's t-test) were used to compare protein expression data between the DR and DS groups, with a p-value  $< 0.05$  set as the threshold for significance. To reduce false positive results, we applied the Benjamini-Hochberg method for multiple hypothesis testing correction, controlling the false discovery rate (FDR), with FDR  $< 0.05$  as the criterion for selecting DEPs. The final screening criteria for DEPs were p-value  $< 0.05$  and  $|\logFC| > 0.5$ .

#### Lentivirus

The plasmid vector pCMV6-AC-GFP (LM- 2069, LMAI Bio, Shanghai, China) was used to construct overexpressing plasmids for HNRNPC and CELF2, which were carried out by Shengsongsheng Biology (Shanghai, China). The plasmid pLKO.1-puro (QYV0024, Beijing Qiyuan Biotechnology Co., Ltd.) was used to construct human HNRNPC-shRNA (sequence 1, 5'– 3': GCGCTTGTCTAAGATCAAATT; sequence 2, 5'– 3': GCCTTCGTTTCAGTATGTTAAT) and human CELF2-shRNA (sequence 1, 5'– 3': GCTCACTTTCTCATTAAGATA; sequence 2, 5'– 3': CGCAGAGTAAAGGTTGTTGTT). The sh-NC (sequence 5'– 3': GCAACAAGATGAAGA GCACCAA) was purchased from Thermo Fisher (USA). The lentiviral constructs oe-HNRNPC, HNRNPC-shRNA (oe-HNRNPC-LTEP-s, hereafter referred to as oe-HNRNPC; HNRNPC-shRNA-LTEP-s, hereafter referred to as sh-HNRNPC), oe-CELF2, CELF2-shRNA (oe-CELF2-LTEP-s, hereafter referred to as oe-CELF2; CELF2-shRNA-LTEP-s, hereafter referred to as sh-CELF2), and control lentivirus (oe-NC-LTEP-s, hereafter

referred to as oe-NC; sh-NC-LTEP-s, hereafter referred to as sh-NC) were constructed based on the HEK293 T cell line (CBP60661, Nanjing Kaibai Biotechnology Co., Ltd., Jiangsu, China). The plasmids and lentivirus packaging were provided by Sheng Gongsheng Biotechnology. The constructed plasmids containing a single luciferase reporter gene (or-NC-luc, oe-HNRNPC-luc, oe-CELF2-luc, sh-NC-luc, sh-HNRNPC-luc, and sh-CELF2-luc) were co-transfected with auxiliary plasmids using Lipofectamine 2000 reagent (11668030, Thermo Fisher, USA) into HEK293 T cells. After verification, amplification, and purification, packaged lentivirus was obtained. For lentivirus-mediated cell transfection,  $5 \times 10^6$  cells were seeded in a 6-well plate. When the cell density reached 70–90%, the medium containing an appropriate amount of packaged lentivirus (MOI = 10, working titer approximately  $5 \times 10^6$  TU/mL) and 5  $\mu$ g/mL polybrene (TR-1003, Merck, USA) was added for transfection. After 4 h of transfection, an equal amount of medium was added to dilute polybrene. Fresh medium was replaced after 24 h of transfection, and the transfection effect was observed by the luciferase reporter gene after 48 h. To obtain stable cell lines, resistance screening was performed using 10  $\mu$ g/mL puromycin (A1113803, Gibco, Grand Island, NY, USA) until the cells no longer died in the puromycin-containing medium. The overexpression and knockdown efficiencies were confirmed by RT-qPCR [64]. Cell grouping was as follows: Resistant group: sh-NC + sh-NC (control group), sh-HNRNPC + sh-NC (transfected with sh-HNRNPC and sh-NC), sh-HNRNPC + sh-CELF2 (transfected with sh-HNRNPC and sh-CELF2). Non-resistant group: oe-NC + oe-NC (control group), oe-HNRNPC + oe-NC (transfected with oe-HNRNPC and oe-NC), oe-HNRNPC + oe-CELF2 (transfected with oe-HNRNPC and oe-CELF2).

#### RT-qPCR

The total RNA from cells or tissues was extracted using Trizol reagent (10296010, Invitrogen, Thermo Fisher, USA). RNA quality and concentration were assessed using a UV-visible spectrophotometer (ND-1000, Nanodrop, Thermo Fisher, USA). Reverse transcription was performed using the PrimeScript™ RT-qPCR kit (RR086A, TaKaRa, Mountain View, CA, USA). Real-time quantitative reverse transcription polymerase chain reaction (RT-qPCR) was carried out on a LightCycler 480 system (Roche Diagnostics, Pleasanton, CA, USA) using SYBR Premix Ex Taq™ (DRR820A, TaKaRa).  $\beta$ -Actin or GAPDH was used as the endogenous control for mRNA amplification. The primer sequences were designed and provided by Shanghai Universal Biotech Co., Ltd. The primer sequences can be found in Table S1. The  $2^{-\Delta\Delta Ct}$  method was used to determine the fold change in target

gene expression between the experimental and control groups, where  $\Delta\Delta Ct = \Delta Ct_{\text{experimental group}} - \Delta Ct_{\text{control group}}$ , and  $\Delta Ct$  is calculated as the difference between the Ct values of the target gene and endogenous control gene [65].

#### MeRIP-qPCR analysis

HNRNPC antibody (PA5-22280, 1:50, Thermo Fisher, USA) was used to immunoprecipitate CELF2 in AML cells, and the m6A levels of CELF2 were assessed using the MeRIP m6A kit (GS-ET-001, Haihe Xi Bio-tech Co., Ltd., Shanghai, China). Methylation-RNA immunoprecipitation (MeRIP) analysis was performed according to the kit's instructions, followed by RNA extraction and RT-qPCR analysis of CELF2 expression [66].

#### M6A dot blot analysis

Cellular RNA samples were denatured under vacuum conditions and then bound to nitrocellulose membranes (7182-004, Cytiva, Shanghai, China). After UV cross-linking, the membrane was stained with methyl blue to check for RNA loading. To detect the level of m6A, the membrane was incubated with an anti-m6A antibody (ab314476, 1:1000, Abcam, UK) overnight at 4 °C, followed by incubation with HRP-conjugated rabbit IgG (ab172730, Abcam, UK) for 60 min at 20 °C. The blot was analyzed using an ECL kit (A38554, Thermo Fisher, USA), and the spots were measured using a chemiluminescence system (Bio-Rad Laboratories, Hercules, CA, USA) [67].

#### Dual-luciferase reporter gene assay

The M6a2 target database (<http://rm2target.canceromics.org/#/home>) predicted that HNRNPC would bind to the CELF2 region. CELF2-WT and CELF2-MUT plasmids were constructed separately and co-transfected with sh-HNRNPC, oe-HNRNPC, and a negative control into AML cells. After 48 h of transfection, the cells were lysed, and the supernatant was collected following centrifugation at 13,000 g for 1 min. The Dual-Luciferase Reporter Gene Assay Kit (ab287865, Abcam, UK) was then used to measure luciferase activity. Each cell sample was mixed with 100  $\mu$ L of firefly luciferase working solution to measure firefly luciferase (FI/Rely luciferase) and 100  $\mu$ L of sea kidney luciferase working solution to measure sea kidney luciferase (Renilla luciferase). The luc2 signal represents firefly luciferase reaction intensity, hRluc-neo represents the reference sea kidney luciferase reaction intensity, and the ratio luc2/hRluc-neo was calculated from the two groups of data [68].

### RNA half-life experiment

Cells were treated with streptomycin D (50–76-0, Sigma Aldrich, USA) at a concentration of 5 µg/mL. After incubation for 0, 4, 8, and 12 h, the cells were collected, and RNA was extracted for RT-qPCR analysis. The degradation rate of RNA was estimated using the formula  $N_t/N_0 = e^{-kt}$  (where  $t$  is the transcription inhibition time,  $N_t$  and  $N_0$  represent the RNA expression levels at time  $t$  and time 0, respectively) [69].

### TUNEL fluorescent staining

For apoptosis analysis, the TUNEL assay was performed following the manufacturer's instructions (11684795910, Roche, USA). Briefly, cells were treated with proteinase K and 3% hydrogen peroxide, then incubated with the TUNEL reaction mixture at 37 °C under humid conditions. Subsequently, cells were labeled with fluorescein-dUTP and counterstained with methyl green. Untreated slices served as a negative control, and the target regions were selected in the images observed under a fluorescence microscope. ImageJ was used for image processing and quantitative analysis to determine the number of positive cells [70].

### CCK-8 assay

AML cells in the logarithmic growth phase were seeded in a 96-well plate at a density of  $5 \times 10^3$  cells per well. At 0, 24, 48, 72, and 96 h, 10 µL of CCK-8 reagent solution (C0038, Beyotime, Shanghai, China) was added to each well, followed by incubation in a humidified CO<sub>2</sub> incubator at 37 °C. The absorbance of each well at 450 nm was measured using a Microplate Reader (abx700005, Beijing Qiwei Yicheng Technology Co., Ltd.) [71]. In the IC<sub>50</sub> assay,  $1 \times 10^4$  AML cells were seeded in a 96-well plate and cultured in RPMI-1640 complete medium. Different concentrations of drugs were added according to the manufacturer's instructions. Cell viability was assessed using the CCK-8 assay, and the concentration of each drug that resulted in 50% growth inhibition (IC<sub>50</sub>) was estimated using relative survival curves [72].

### Transwell assay

Cell culture was performed using Transwell polycarbonate membranes (CLS3422, Corning, USA). AML cell suspension was added to the upper chamber of the Transwell insert at a density of  $2 \times 10^4$  cells per well in serum-free medium, while medium containing 10% fetal bovine serum was added to the lower chamber. After 24 h of incubation, non-migrating cells in the upper chamber were removed, and the cells that migrated through the pores were fixed and stained with 0.1% crystal violet

(C0121, Beyotime, Shanghai, China). Eight random fields were observed under an inverted microscope (XDS-900, Caikon, Shanghai, China) [73].

### Multicellular spheroid (MCS) formation

A total of 1000 AML cells/spheroids were inoculated into 35-well or 81-well agarose tubes (A6013, Sigma-Aldrich, USA), generated by 3D Petri dishes (Microtissues<sup>®</sup>, Microtissues Inc., RI, USA). One minute after cell seeding, 1 mL (for 35-well) or 2 mL (for 81-well) of cell culture medium was added, and the cells were cultured at 37 °C and 5% CO<sub>2</sub> to form cancer cell spheroids.

To assess the invasive ability of AML cells in different treatment groups, Type I collagen (CC050, Sigma-Aldrich, USA) was added. First, collagen was neutralized to a pH of 7.0–8.0 and then filled into the agarose tubes. After incubation for 4 min, the agarose tube was inverted (including the co-culture with buried collagen) and further incubated for 1 h. The tube was then flipped, and RPMI medium containing 5% FBS and 1% Pen/Strep was added. Invasion assays were performed for 2 days, and images were captured using an inverted microscope until viable cells were recovered from the collagen matrix.

After 24 h of co-culturing, the spheroids were washed, stained, and fixed using a viability/cytotoxicity assay kit (30002, Biotium, USA). Images were acquired through confocal microscopy, scanning from the top to the middle of the spheroid with 5 µm intervals using Z-stack and presented as maximum intensity projection. The surface display (2.5D) was obtained using Zeiss image processing software. Image J software was utilized to measure the total cell area for each dye in order to quantify live/dead cells.

### LC-MS (liquid chromatography-mass spectrometry) coupling method

Samples of drug-resistant and non-resistant cells were collected and transferred to 1.5 mL polypropylene tubes, with 300 µL of each sample. Then, 900 µL of an 80% methanol solution (67-56-1, Sigma-Aldrich, USA) mixed with 0.1% formic acid (64-18-6, Sigma-Aldrich, USA) was added. The tubes were centrifuged at 12,000 g for 10 min, and the supernatant was transferred to the vials of an autosampler.

Metabolomics analysis was conducted using the LC20 ultra-high-performance liquid chromatography system (SHIMADZU, Japan) coupled with the Triple TOF-6600 mass spectrometer (AB Sciex, USA). Chromatographic separation was performed using a Waters ACQUITY UPLC HSS T3 C18 column (100 × 2.1 mm, 1.8 µm) at a column temperature of 40 °C and a flow rate of 0.4 mL/min. The mobile phase consisted of an acetonitrile (75-05-8, Sigma-Aldrich, USA) and a water solution

containing 0.1% formic acid. The gradient elution program for mobile phase B was as follows: 5% from 0.0 to 11.0 min, 90% from 11.0 to 12.0 min, and 5% from 12.1 to 14 min. The eluent was directly introduced to the mass spectrometer without splitting [74].

Mass spectrometry in positive/negative ion modes was performed under the following conditions: ionization voltage of 5500 V, capillary temperature of 550 °C, nebulizer gas flow rate of 50 psi, and auxiliary heating gas flow rate of 60 psi. The preprocessed data was analyzed using orthogonal partial least squares-discriminant analysis (OPLS-DA) and permutation testing (100 permutations) to prevent overfitting. Metabolites with a VIP score >1 and a P-value <0.05 in the OPLS-DA model were identified as differential metabolites (DMs). Furthermore, combined with univariate analysis, metabolites with fold changes  $\geq 2$  and  $\leq 0.5$  and a Student's t-test P-value <0.05 were selected as the final differential metabolites. Metabolic pathways related to the identified metabolites were determined using MetaboAnalyst (version 5.0) [75].

#### Western blot

Total protein was extracted from cells and tissues using enhanced RIPA lysis buffer (AR0108, Wuhan Bode Company, Wuhan, China) containing proteinase inhibitors. The protein concentration was measured using a BCA protein quantification kit (AR1189, Wuhan Bode Company, Wuhan, China). Protein samples were separated by SDS-PAGE, followed by transfer onto a PVDF membrane. After blocking with 5% BSA (9048 -46- 8, Sigma-Aldrich, USA) at room temperature for 1 h, the membranes were incubated overnight at 4 °C with the respective diluted primary antibodies (refer to Table S2 for detailed information on the primary antibodies). The membranes were then washed three times with PBST (5 min per wash) and incubated at room temperature for 1 h with either Anti-Mouse-HRP secondary antibody (Cat # 7076, 1/5000; CST, USA) or Anti-Rabbit-HRP secondary antibody (Cat # 7074, 1/5000; CST, USA). The membranes were washed again with PBST (5 min per wash). After removing PBST, an appropriate amount of ECL working solution was added, and the membranes were incubated at room temperature for 1 min. Excess ECL reagent was removed, and the membranes were sealed with plastic wrap, placed in a dark box, and exposed to X-ray film for 5–10 min for visualization and development. The bands in the Western blot images were quantified for grayscale using Image J analysis software, with  $\beta$ -Actin or GAPDH as the reference proteins [76, 77].

#### Detection of total ROS and mitochondrial ROS

To detect reactive oxygen species (ROS), we utilized the fluorescent dye 2',7'-dichlorodihydrofluorescein diacetate

(DCFDA) (HY-D0940, Abcam, UK), which enters cells and forms a green fluorescent compound, dichlorofluorescein (DCF), upon interaction with ROS molecules. In brief, a methanol stock solution of DCFDA (10 mM) was prepared and further diluted with culture medium to obtain a working solution of 100  $\mu$ M. AML cells ( $2 \times 10^4$ ) were seeded on glass coverslips in a six-well plate overnight. The following day, cells were treated with H<sub>2</sub>O<sub>2</sub> (200  $\mu$ M) for 24 h. After treatment, coverslips were washed with cold Hank's Balanced Salt Solution (HBSS) (H8264, Sigma Aldrich, USA) and incubated with 100  $\mu$ M of DCFDA at 37 °C for 30 min. Following a wash with 1  $\times$  PBS, coverslips were mounted on slides. Images were analyzed using a multiphoton confocal microscope (A1R, Nikon, USA) with a  $\times 100$  objective and Nikon's NIS Element imaging software, while positive cells were counted using Image J analysis software.

For the evaluation of superoxide compounds (SOX) in mitochondria, we employed the red fluorescent compound mito-SOX (M36008, Thermo Fisher, USA). AML cells ( $2 \times 10^4$ ) were seeded on glass coverslips in a six-well plate overnight. The next day, cells were treated with H<sub>2</sub>O<sub>2</sub> (200  $\mu$ M) for 24 h. Subsequently, coverslips were washed with cold 1  $\times$  PBS and incubated with a working solution of 2  $\mu$ M mito-SOX at 37 °C for 30 min. After washing with 1  $\times$  PBS, coverslips were mounted on slides. Images were analyzed using a multiphoton confocal microscope with a  $\times 100$  objective, Nikon's NIS Element imaging software, and Image J analysis software for counting positive cells [78].

#### MitoTracker staining

MitoTracker (M7513, Thermo Fisher, USA) was utilized to label mitochondria in AML cells. AML cells were treated and co-incubated with MitoTracker (200 nM) at 37 °C for 45 min. The fluorescent signal was detected using confocal fluorescence microscopy [79].

#### Metabolic measurements

The Seahorse XFe96 Extracellular Flux Analyzer (Agilent Technologies) was employed for metabolic analysis. The extracellular acidification rate (ECAR) and oxygen consumption rate (OCR) were calculated for each well. The following concentrations of injection compounds were used to induce XF glycolytic stress or XF cell Mito testing: 10 mM glucose (50–99- 7, Sigma-Aldrich, USA), 2  $\mu$ M oligomycin (1404 -19- 9, Sigma-Aldrich, USA), 50 mM 2-deoxy-d-glucose (2-DG) (154 -17- 6, Sigma-Aldrich, USA), 1  $\mu$ M carbonyl cyanide- 4-(trifluoromethoxy)phenylhydrazone (FCCP) (370–86 -5, Sigma-Aldrich, USA), and 0.5  $\mu$ M rotenone (83 -79- 4, Sigma-Aldrich, USA). The XF Glycolytic Stress or XF Cell Mito Test Kit was purchased from Agilent Technologies (USA) [80].

### Subcutaneous tumorigenesis in nude mice with AML cells

To establish an AML subcutaneous tumor model, AML-Luc cells ( $2 \times 10^6$ ) labeled with luciferase enzyme (61970-00-1, Sigma-Aldrich, USA) were injected subcutaneously into the left abdominal region of 6-week-old female BALB/c-nu mice. A total volume of 200  $\mu$ L AML-Luc cells was used. The tumor growth was visually observed, and 15 days after transplantation, treatment was initiated using Cytarabine (dose of 3 mg/kg/day) administered through tail vein injection until the mice were sacrificed [81, 82]. Live fluorescence imaging of the mice was performed using the IVIS Lumina Series III in vivo imaging system (PerkinElmer, USA) at 15, 25, and 30 days post-transplantation. Brief anesthesia was administered to the mice prior to imaging to ensure they remained still [83].

After 30 days of subcutaneous tumor growth, the mice were deeply anesthetized with isoflurane, and the tumor tissue was collected for measurement, RT-qPCR, Western blot, and immunohistochemical experiments.

The animals were divided into different groups as follows: Group 1 (G1): oe-NC + oe-NC + DMSO (KG-1 cells transfected with negative control vector oe-NC, followed by subcutaneous injection and 15 days later, tail vein injection of DMSO as a control). Group 2 (G2): oe-NC + oe-NC + Cytarabine (KG-1 cells transfected with negative control vector oe-NC, followed by subcutaneous injection and 15 days later, tail vein injection of Cytarabine). Group 3 (G3): oe-HNRNPC + oe-NC + DMSO (KG-1 cells transfected with oe-HNRNPC and oe-NC, followed by subcutaneous injection and 15 days later, tail vein injection of DMSO). Group 4 (G4): oe-HNRNPC + oe-NC + Cytarabine (KG-1 cells transfected with oe-HNRNPC and oe-NC, followed by subcutaneous injection and 15 days later, tail vein injection of Cytarabine). Group 5 (G5): oe-HNRNPC + oe-CELF2 + Cytarabine (KG-1 cells transfected with oe-HNRNPC and oe-CELF2, followed by subcutaneous injection and 15 days later, tail vein injection of Cytarabine).

Group 1/DR (G1/DR): sh-NC + sh-NC + DMSO (KG-1/DR cells transfected with negative control vector sh-NC, followed by subcutaneous injection and 15 days later, tail vein injection of DMSO as a control). Group 2/DR (G2/DR): sh-NC + sh-NC + Cytarabine (KG-1/DR cells transfected with negative control vector sh-NC, followed by subcutaneous injection and 15 days later, tail vein injection of Cytarabine). Group 3/DR (G3/DR): sh-HNRNPC + sh-NC + DMSO (KG-1/DR cells transfected with sh-HNRNPC and sh-NC, followed by subcutaneous injection and 15 days later, tail vein injection of DMSO). Group 4/DR (G4/DR): sh-HNRNPC + sh-NC + Cytarabine (KG-1/DR cells transfected with sh-HNRNPC and sh-NC, followed by subcutaneous injection and 15 days later, tail vein injection of Cytarabine). Group 5/DR (G5/

DR): sh-HNRNPC + sh-CELF2 + Cytarabine (KG-1/DR cells transfected with sh-HNRNPC and sh-CELF2, followed by subcutaneous injection and 15 days later, tail vein injection of Cytarabine).

### Immunohistochemistry

The tissue or cells under investigation were fixed and embedded. The embedded tissue was then sectioned and subjected to dewaxing treatment, which removes the wax from the slides, making them hydrophilic and facilitating subsequent immunostaining procedures. The dewaxed tissue sections were treated with specific antibodies, including Ki67 antibody (SAB5700770, 1:200; Sigma Aldrich, USA), GLUT1 antibody (MA5-31960, 1:200; Thermo Fisher, USA), and HK2 antibody (PA5-29326, 1:200; Thermo Fisher, USA). Anti-Rabbit-HRP secondary antibody (12-348, 1:1000; Sigma Aldrich, USA) was applied to the sections. The binding sites between the secondary antibody and the primary antibodies were visualized using a DAB staining solution (ab64238, Abcam, USA). The stained tissue sections were dewaxed, mounted on slides, and observed under a microscope to record the expression patterns. The criteria for evaluating staining results involved randomly selecting five regions of interest and counting the number of positively stained cells within each region [84].

### Statistical analysis

Statistical analysis for this study was performed using GraphPad Prism (9.0) and R (4.3.0) software. Continuous data were presented as mean  $\pm$  standard deviation (Mean  $\pm$  SD), and the unpaired t-test was employed to compare the two groups. One-way analysis of variance (ANOVA) was used for comparisons among multiple groups, with homogeneity of variances assessed using the Levene test. In cases of homogeneous variance, Dunnett's t-test and LSD-t test were applied for pairwise comparisons. A significance level of  $p < 0.05$  was considered statistically significant [85].

### Supplementary Information

The online version contains supplementary material available at <https://doi.org/10.1186/s13578-025-01386-x>.

Supplementary Material 1: Figure S1. Generating AML mouse model. Schematic diagram of generating AML mouse model; Comparison of body weight difference between normal mice and AML mice, with a group size of 30 mice; Measurement of WBC, RBC, and PLT counts in peripheral blood of mice, with a group size of 30 mice; Statistical analysis of mouse body weights, with a group size of 25 mice; Measurement of WBC, RBC, and PLT counts in peripheral blood of mice, with a group size of 25 mice; Measurement of WBC, RBC, and PLT counts in peripheral blood of mice, with a group size of 10 mice in the weight gain group and 6 mice in the weight loss group; Measurement of CD11b, CD41a, and Ter119 in mouse bone marrow using flow cytometry, with the number of mice being 6 in each group. The right panel shows the MFI statistical

graph:Immunofluorescence detection of CD11b, CD41a, and Ter119 expression in mouse bone marrow, Bar = 50  $\mu$ m. The right panel shows the positive cell statistical graph, with 6 mice in each group. Values are expressed as mean  $\pm$  standard deviation, with differences between two groups analyzed using t-tests. \* represents  $p < 0.05$ , \*\* represents  $p < 0.01$ , and \*\*\* represents  $p < 0.001$ .

Supplementary Material 2: Figure S2. Quality control, filtering, and principal component analysis of scRNA-seq data. Violin plots displaying the number of genes, mRNA molecules, and mitochondrial gene percentage for each cell in the scRNA-seq data; Scatter plots showing the correlation between filtered data nCount\_RNA and percent. Mt, as well as nCount\_RNA and nFeature\_RNA; Variance analysis to select highly variable genes, where red represents the top 2000 highly variable genes, and black represents low variable genes. The top 10 gene names in highly variable genes are labeled; Cell cycle status of each cell in the scRNA-seq data, with S.Score representing S phase and G2M. Score representing G2M phase; Heatmap of the top 20 genes associated with PC\_1—PC\_6 in PCA, with yellow indicating upregulated expression and purple indicating downregulated expression; Distribution of cells before batch correction in PC\_1 and PC\_2, with each point representing a cell.

Supplementary Material 3: Figure S3. Clustering of scRNA-seq data cells. Diagram of the batch correction process using Harmony, with the x-axis representing the number of interactions; Distribution of standard deviations for PCs, where important PCs have a larger standard deviation; Distribution of cells after batch correction in PC\_1 and PC\_2, with each point representing a cell; UMAP visualization of clustering results, showing the aggregation and distribution of cells, with each color representing a cluster; Two-dimensional UMAP visualization of cell clusters from the DR and DS groups, with blue representing DR samples and red representing DS samples; UMAP visualization showing the expression of marker genes in each cell subgroup; T-test analysis of the difference in cell content between DS and DR groups, with P-values, with differences between two groups analyzed using t-tests. \*\* represents  $p < 0.01$ , and \*\*\* represents  $p < 0.001$ .

Supplementary Material 4: Figure S4. T-SNE clustering tree diagram for scRNA-seq data. The Clustree package displays the clustering results at different resolutions.

Supplementary Material 5: Figure S5. Cell communication and cell trajectory analysis in scRNA-seq dataset. Displaying cell-to-cell communication separately; Comparing the total number and intensity of signaling interactions between the DS and DR groups; Circle plot showing the changes in cell communication in DR compared to the DS group, with red indicating upregulation and blue indicating downregulation; Trajectory skeleton diagrams with pseudo-temporal coloring and cell type coloring, with each point representing a cell; UMAP plot showing cell clustering of AML cell populations; Heatmap of the top 5 correlated genes in three stages of cells; Cell proportion bar graph; T-test analysis of the difference in cell content between DS and DR groups, with P-values, with differences between two groups analyzed using t-tests. \*\* representing  $p < 0.01$ , and \*\*\* representing  $p < 0.001$ .

Supplementary Material 6: Figure S6. Validation of HNRNPC and CELF2 relationship in the M6a2 target database. M6a2 target database validation of CELF2 as a substrate of HNRNPC in THP1 cell line; M6a2 target database prediction of HNRNPC binding to region chr10: 11019141–11019176 of CELF2.

Supplementary Material 7: Figure S7. RT-PCR validation in AML cells. Validation of low-efficiency knockdown of HNRNPC in non-resistant AML cells; Validation of overexpression efficiency of HNRNPC in non-resistant AML cells; Expression levels of HNRNPC and CELF2 in drug-resistant AML cells; Expression levels of HNRNPC and CELF2 in non-resistant AML cells. All cell experiments were repeated three times, and values are expressed as mean  $\pm$  standard deviation, with differences between two groups analyzed using t-tests. \* represents  $p < 0.05$ , \*\* represents  $p < 0.01$ , and \*\*\* represents  $p < 0.001$ .

Supplementary Material 8: Figure S8. Construction of drug-resistant cell lines and IC50 determination. Schematic diagram of drug-resistant cell line construction; Viability of drug-resistant cells and parental cells after 48 h at specified doses measured using CCK-8 assay and calculation of Cytarabine IC50; Expression levels of HNRNPC and CELF2 in non-resistant and drug-resistant AML cells; Viability of different groups of cells after 48 h at specified doses measured using CCK-8 assay, and calculation of Cytarabine IC50. All cell experiments were repeated three times, and values are expressed as mean  $\pm$  standard deviation, with differences between two groups analyzed using t-tests. \* represents  $p < 0.05$ , \*\* represents  $p < 0.01$ , and \*\*\* represents  $p < 0.001$ .

Supplementary Material 9.

## Acknowledgements

None.

## Author contributions

X.M. and H.L. performed experiments, analyzed data, and drafted the manuscript. Z.Z., C.L., M.W., L.Z., Y.Z., and H.S. assisted with experiments and data interpretation. F.W. provided technical support and contributed to the experimental design. J.H. conceived the study, supervised the project, revised the manuscript, and secured funding. All authors reviewed and approved the final manuscript.

## Funding

This study was supported by Shanxi Province Science Foundation (20210302124333), Shanxi "1331" Project, Taiyuan Institute of Technology Scientific Research Initial Funding, Program for the Discipline Leaders of Taiyuan Institute of Technology.

## Data availability

All data can be provided as needed.

## Declarations

### Ethics approval and consent to participate

All animal experiments were approved by the Animal Ethics Committee of Taiyuan Institute of Technology.

### Competing interests

The author declares no conflict of interest.

Received: 17 December 2024 Accepted: 29 March 2025

Published online: 16 May 2025

## References

- Chen Y, Hoffmeister LM, Zaun Y, et al. Acute myeloid leukemia-induced remodeling of the human bone marrow niche predicts clinical outcome. *Blood Adv*. 2020;4(20):5257–68. <https://doi.org/10.1182/bloodadvances.2020001808>.
- Cao H, Xiao J, Reeves ME, et al. Discovery of proangiogenic CD44+ mesenchymal cancer stem cells in an acute myeloid leukemia patient's bone marrow. *J Hematol Oncol*. 2020. <https://doi.org/10.1186/s13045-020-00899-x>.
- Wang J, Zhuo Z, Wang Y, et al. Identification and validation of a prognostic risk-scoring model based on ferroptosis-associated cluster in acute myeloid leukemia. *Front Cell Dev Biol*. 2022. <https://doi.org/10.3389/fcell.2021.800267>.
- Li R, Wu S, Wu X, et al. Immune-related lncRNAs can predict the prognosis of acute myeloid leukemia. *Cancer Med*. 2021;11(3):888–99. <https://doi.org/10.1002/cam4.4487>.
- Pelcovits A, Niroula R. Acute myeloid leukemia: a review. *R I Med J*. 2020;103(3):38–40.

6. Shimony S, Stahl M, Stone RM. Acute myeloid leukemia: 2023 update on diagnosis, risk-stratification, and management. *Am J Hematol*. 2023;98(3):502–26. <https://doi.org/10.1002/ajh.26822>.
7. Newell LF, Cook RJ. Advances in acute myeloid leukemia. *BMJ*. 2021. <https://doi.org/10.1136/bmj.n2026>.
8. Cao R, Zhang J, Jiang L, et al. Comprehensive analysis of prognostic alternative splicing signatures in oral squamous cell carcinoma. *Front Oncol*. 2020. <https://doi.org/10.3389/fonc.2020.01740>.
9. Liu D, Luo X, Xie M, et al. HNRNPC downregulation inhibits IL-6/STAT3-mediated HCC metastasis by decreasing HIF1A expression. *Cancer Sci*. 2022;113(10):3347–61. <https://doi.org/10.1111/cas.15494>.
10. Yuan F, Cai X, Cong Z, et al. Roles of the m6A modification of RNA in the glioblastoma microenvironment as revealed by single-cell analyses. *Front Immunol*. 2022. <https://doi.org/10.3389/fimmu.2022.798583>.
11. Cai Y, Lyu T, Li H, et al. LncRNA CEBPA-DT promotes liver cancer metastasis through DDR2/ $\beta$ -catenin activation via interacting with hnRNPC. *J Exp Clin Cancer Res*. 2022. <https://doi.org/10.1186/s13046-022-02544-6>.
12. Jin S, Li M, Chang H, et al. The m6A demethylase ALKBH5 promotes tumor progression by inhibiting RIG-I expression and interferon alpha production through the IKK $\epsilon$ /TBK1/IRF3 pathway in head and neck squamous cell carcinoma. *Mol Cancer*. 2022. <https://doi.org/10.1186/s12943-022-01572-2>.
13. Lv W, Tan Y, Xiong M, et al. Analysis and validation of m6A regulatory network: a novel circBACH2/has-miR-944/HNRNPC axis in breast cancer progression. *J Transl Med*. 2021. <https://doi.org/10.1186/s12967-021-03196-4>.
14. Theilgaard-Mönch K, Boultonwood J, Ferrari S, et al. Gene expression profiling in MDS and AML: potential and future avenues. *Leukemia*. 2011;25(6):909–20. <https://doi.org/10.1038/leu.2011.48>.
15. Bacher U, Kohlmann A, Haferlach C, Haferlach T. Gene expression profiling in acute myeloid leukaemia (AML). *Best Pract Res Clin Haematol*. 2009;22(2):169–80. <https://doi.org/10.1016/j.beha.2009.04.003>.
16. Bian X, Jiang H, Meng Y, Li Y-P, Fang J, Lu Z. Regulation of gene expression by glycolytic and gluconeogenic enzymes. *Trends Cell Biol*. 2022;32(9):786–99. <https://doi.org/10.1016/j.tcb.2022.02.003>.
17. Li Z, Zhang H. Reprogramming of glucose, fatty acid and amino acid metabolism for cancer progression. *Cell Mol Life Sci*. 2015;73(2):377–92. <https://doi.org/10.1007/s00018-015-2070-4>.
18. Hancio T, Mazzoccoli L, Guimaraes G, et al. The pterocarpanquinone LQB-118 compound induces apoptosis of cytarabine-resistant acute myeloid leukemia cells. *Int J Oncol*. 2021. <https://doi.org/10.3892/ijo.2021.5204>.
19. Doycheva I, Ehrmann DA. Nonalcoholic fatty liver disease and obstructive sleep apnea in women with polycystic ovary syndrome. *Fertil Steril*. 2022;117(5):897–911. <https://doi.org/10.1016/j.fertnstert.2022.03.020>.
20. Brown E, Hydes T, Hamid A, Cuthbertson DJ. Emerging and established therapeutic approaches for nonalcoholic fatty liver disease. *Clin Ther*. 2021;43(9):1476–504. <https://doi.org/10.1016/j.clinthera.2021.07.013>.
21. Döhner H, Weisdorf DJ, Bloomfield CD. Acute myeloid leukemia. *N Engl J Med*. 2015;373(12):1136–52. <https://doi.org/10.1056/nejmra1406184>.
22. Yan D, Wei H, Lai X, et al. Co-delivery of homoharringtonine and doxorubicin boosts therapeutic efficacy of refractory acute myeloid leukemia. *J Control Release*. 2020;327:766–78. <https://doi.org/10.1016/j.jconrel.2020.09.031>.
23. Driss V, Quesnel B, Brinster C. Monocyte chemoattractant protein 1 (MCP-1/CCL2) contributes to thymus atrophy in acute myeloid leukemia. *Eur J Immunol*. 2014;45(2):396–406. <https://doi.org/10.1002/eji.20144736>.
24. He Q, Yang C, Xiang Z, et al. LINC00924-induced fatty acid metabolic reprogramming facilitates gastric cancer peritoneal metastasis via hnRNPC-regulated alternative splicing of Mnk2. *Cell Death Dis*. 2022. <https://doi.org/10.1038/s41419-022-05436-x>.
25. Wu Z, Zuo X, Zhang W, et al. m6A-modified circTET2 interacting with HNRNPC regulates fatty acid oxidation to promote the proliferation of chronic lymphocytic leukemia. *Adv Sci*. 2023. <https://doi.org/10.1002/advs.202304895>.
26. Shi M, Yang R, Lin J, et al. LncRNA-SNHG16 promotes proliferation and migration of acute myeloid leukemia cells via PTEN/PI3K/AKT axis through suppressing CELF2 protein. *J Biosci*. 2021;46:4.
27. Guo D, Zhang A, Suo M, Wang P, Liang Y. ELK1-Induced upregulation of long non-coding TNK2-AS1 promotes the progression of acute myeloid leukemia by EZH2-mediated epigenetic silencing of CELF2. *Cell Cycle*. 2022;22(1):117–30. <https://doi.org/10.1080/15384101.2022.2109898>.
28. Huang XT, Li JH, Zhu XX, et al. HNRNPC impedes m6A-dependent anti-metastatic alternative splicing events in pancreatic ductal adenocarcinoma. *Cancer Lett*. 2021;518:196–206. <https://doi.org/10.1016/j.canlet.2021.07.016>.
29. Martínez-Reyes I, Chandel NS. Cancer metabolism: looking forward. *Nat Rev Cancer*. 2021;21(10):669–80. <https://doi.org/10.1038/s41568-021-00378-6>.
30. Chou MY, Yang MH. Interplay of immunometabolism and epithelial-mesenchymal transition in the tumor microenvironment. *IJMS*. 2021;22(18):9878. <https://doi.org/10.3390/ijms22189878>.
31. Hanahan D, Weinberg RA. Hallmarks of cancer: the next generation. *Cell*. 2011;144(5):646–74. <https://doi.org/10.1016/j.cell.2011.02.013>.
32. Lunt SY, Vander Heiden MG. Aerobic glycolysis: meeting the metabolic requirements of cell proliferation. *Annu Rev Cell Dev Biol*. 2011;27(1):441–64. <https://doi.org/10.1146/annurev-cellbio-092910-154237>.
33. Cheng C, Yuan F, Chen XP, et al. Inhibition of Nrf2-mediated glucose metabolism by brusatol synergistically sensitizes acute myeloid leukemia to Ara-C. *Biomed Pharmacother*. 2021;142: 111652. <https://doi.org/10.1016/j.biopha.2021.111652>.
34. Xu W, Janocha AJ, Erzurum SC. Metabolism in pulmonary hypertension. *Annu Rev Physiol*. 2021;83(1):551–76. <https://doi.org/10.1146/annurev-physiol-031620-123956>.
35. Thol F, Ganser A. Treatment of relapsed acute myeloid leukemia. *Curr Treat Options in Oncol*. 2020. <https://doi.org/10.1007/s11864-020-00765-5>.
36. Bakhtiyari M, Liaghat M, Aziziyan F, et al. The role of bone marrow micro-environment (BMM) cells in acute myeloid leukemia (AML) progression: immune checkpoints, metabolic checkpoints, and signaling pathways. *Cell Commun Signal*. 2023. <https://doi.org/10.1186/s12964-023-01282-2>.
37. Vitale I, Manic G, Coussens LM, Kroemer G, Galluzzi L. Macrophages and metabolism in the tumor microenvironment. *Cell Metab*. 2019;30(1):36–50. <https://doi.org/10.1016/j.cmet.2019.06.001>.
38. Zanotelli MR, Zhang J, Reinhart-King CA. Mechanoresponsive metabolism in cancer cell migration and metastasis. *Cell Metab*. 2021;33(7):1307–21. <https://doi.org/10.1016/j.cmet.2021.04.002>.
39. Chen JJ, Lu TZ, Wang T, et al. The m6A reader HNRNPC promotes glioma progression by enhancing the stability of IRAK1 mRNA through the MAPK pathway. *Cell Death Dis*. 2024. <https://doi.org/10.1038/s41419-024-06736-0>.
40. Li J, Xian L, Zhu Z, et al. Role of CELF2 in ferroptosis: potential targets for cancer therapy (Review). *Int J Mol Med*. 2023. <https://doi.org/10.3892/ijmm.2023.5291>.
41. Taciak B, Pruszyńska I, Kiraga L, Bialasek M, Krol M. Wnt signaling pathway in development and cancer. *J Physiol Pharmacol*. 2018;69(2):185–96. <https://doi.org/10.26402/jpp.2018.2.07>.
42. Skoda AM, Simovic D, Karin V, Kardum V, Vranic S, Serman L. The role of the Hedgehog signaling pathway in cancer: a comprehensive review. *Bosn J of Basic Med Sci*. 2018;18(1):8–20. <https://doi.org/10.17305/bjbm.2018.2756>.
43. Glaviano A, Foo ASC, Lam HY, et al. PI3K/AKT/mTOR signaling transduction pathway and targeted therapies in cancer. *Mol Cancer*. 2023. <https://doi.org/10.1186/s12943-023-01827-6>.
44. Yeung CCS, Radich J. Predicting chemotherapy resistance in AML. *Curr Hematol Malig Rep*. 2017;12(6):530–6. <https://doi.org/10.1007/s11899-017-0378-x>.
45. Konopleva MY. Mechanisms for resistance in AML insights into molecular pathways mediating resistance to venetoclax. *Best Pract Res Clin Haematol*. 2021;34(1): 101251. <https://doi.org/10.1016/j.beha.2021.101251>.
46. Stelmach P, Trumpp A. Leukemic stem cells and therapy resistance in acute myeloid leukemia. *Haematol*. 2023;108(2):353–66. <https://doi.org/10.3324/haematol.2022.280800>.
47. Nehrbas J, Butler JT, Chen DW, Kurre P. Extracellular vesicles and chemotherapy resistance in the AML microenvironment. *Front Oncol*. 2020. <https://doi.org/10.3389/fonc.2020.00090>.
48. Ma Y, Zhou Q, Zhao P, et al. Effect of transferrin glycation induced by high glucose on HK-2 cells in vitro. *Front Endocrinol*. 2023. <https://doi.org/10.3389/fendo.2022.1009507>.
49. Mopin A, Leprière F, Sebda S, et al. Detection of residual and chemoresistant leukemic cells in an immune-competent mouse model of acute myeloid leukemia: potential for unravelling their interactions with

- immunity. *PLoS ONE*. 2022;17(4): e0267508. <https://doi.org/10.1371/journal.pone.0267508>.
50. Driss V, Leprêtre F, Briche I, et al. Sub-clonal analysis of the murine C1498 acute myeloid leukaemia cell line reveals genomic and immunogenic diversity. *Immunol Lett*. 2017;192:27–34. <https://doi.org/10.1016/j.imlet.2017.10.004>.
  51. Tsuchida T, Lee YA, Fujiwara N, et al. A simple diet- and chemical-induced murine NASH model with rapid progression of steatohepatitis, fibrosis and liver cancer. *J Hepatol*. 2018;69(2):385–95. <https://doi.org/10.1016/j.jhep.2018.03.011>.
  52. Fang W, Zhou T, Shi H, et al. Progranulin induces immune escape in breast cancer via up-regulating PD-L1 expression on tumor-associated macrophages (TAMs) and promoting CD8+ T cell exclusion. *J Exp Clin Cancer Res*. 2021. <https://doi.org/10.1186/s13046-020-01786-6>.
  53. Zhang T, Guan G, Zhang J, et al. E2F1-mediated AUF1 upregulation promotes HCC development and enhances drug resistance via stabilization of AKR1B10. *Cancer Sci*. 2022;113(4):1154–67. <https://doi.org/10.1111/cas.15272>.
  54. Zhou KX, Huang S, Hu LP, et al. Increased nuclear transporter KPNA2 contributes to tumor immune evasion by enhancing PD-L1 expression in PDAC. *J Immunol Res*. 2021;2021:1–13. <https://doi.org/10.1155/2021/6694392>.
  55. Zhong G, Wang Q, Wang Y, et al. scRNA-seq reveals ATPIF1 activity in control of T cell antitumor activity. *Oncol Immunology*. 2022. <https://doi.org/10.1080/2162402x.2022.2114740>.
  56. Li W, Zhang S, Liu J, Liu Y, Liang Q. Vitamin K2 stimulates Mc3T3-E1 osteoblast differentiation and mineralization through autophagy induction. *Mol Med Report*. 2019. <https://doi.org/10.3892/mmr.2019.10040>.
  57. Keefe F, Monzón-Sandoval J, Rosser AE, Webber C, Li M. Single-cell transcriptomics reveals conserved regulatory networks in human and mouse interneuron development. *IJMS*. 2023;24(9):8122. <https://doi.org/10.3390/ijms24098122>.
  58. Hao Y, Hao S, Andersen-Nissen E, et al. Integrated analysis of multimodal single-cell data. *Cell*. 2021;184(13):3573–3587.e29. <https://doi.org/10.1016/j.cell.2021.04.048>.
  59. Ma L, Hernandez MO, Zhao Y, et al. Tumor cell biodiversity drives microenvironmental reprogramming in liver cancer. *Cancer Cell*. 2019;36(4):418–430.e6. <https://doi.org/10.1016/j.ccell.2019.08.007>.
  60. Ritchie ME, Phipson B, Wu D, et al. limma powers differential expression analyses for RNA-seq and microarray studies. *Nucleic Acids Res*. 2015;43(7):e47–e47. <https://doi.org/10.1093/nar/gkv007>.
  61. Liu Y, Fang Y, Bao L, Wu F, Wang S, Hao S. Intercellular communication reveals therapeutic potential of epithelial-mesenchymal transition in triple-negative breast cancer. *Biomolecules*. 2022;12(10):1478. <https://doi.org/10.3390/biom12101478>.
  62. Liu XS, Zhou LM, Yuan LL, et al. NPM1 is a prognostic biomarker involved in immune infiltration of lung adenocarcinoma and associated with m6A modification and glycolysis. *Front Immunol*. 2021. <https://doi.org/10.3389/fimmu.2021.724741>.
  63. Chen J, Li S, Ge Y, et al. iTRAQ and PRM-based proteomic analysis provides new insights into mechanisms of response to triple therapy in patients with rheumatoid arthritis. *JIR*. 2021;14:6993–7006. <https://doi.org/10.2147/jirs.340351>.
  64. Yan R, Zhang L, Xia N, Liu Q, Sun H, Guo H. Knockdown of augmenter of liver regeneration in HK-2 cells inhibits inflammation response via the mitogen-activated protein kinase signaling pathway. *Inflamm Res*. 2015;64(6):453–62. <https://doi.org/10.1007/s00011-015-0825-x>.
  65. Schwarz AP, Malygina DA, Kovalenko AA, Trofimov AN, Zaitsev AV. Multiplex qPCR assay for assessment of reference gene expression stability in rat tissues/samples. *Mol Cell Probes*. 2020;53: 101611. <https://doi.org/10.1016/j.mcp.2020.101611>.
  66. Zhang Y, Wang D, Wu D, Zhang D, Sun M. Long noncoding RNA KCNMB2-AS1 stabilized by N6-methyladenosine modification promotes cervical cancer growth through acting as a competing endogenous RNA. *Cell Transplant*. 2020;29:096368972096438. <https://doi.org/10.1177/0963689720964382>.
  67. Qi Y, Yao R, Zhang W, Cui Q. KAT1 triggers YTHDF2-mediated ITGB1 mRNA instability to alleviate the progression of diabetic retinopathy. *Pharmacol Res*. 2021;170: 105713. <https://doi.org/10.1016/j.phrs.2021.105713>.
  68. Wang L, Wang Z, Shi J, et al. Inhibition of proprotein convertase subtilisin/kexin type 9 attenuates neuronal apoptosis following focal cerebral ischemia via apolipoprotein E receptor 2 downregulation in hyperlipidemic mice. *Int J Mol Med*. 2018. <https://doi.org/10.3892/ijmm.2018.3797>.
  69. Yang Z, Wang T, Wu D, Min Z, Tan J, Yu B. RNA N6-methyladenosine reader IGF2BP3 regulates cell cycle and angiogenesis in colon cancer. *J Exp Clin Cancer Res*. 2020. <https://doi.org/10.1186/s13046-020-01714-8>.
  70. Su Y, Quan C, Li X, Shi Y, Duan P, Yang K. Mutual promotion of apoptosis and autophagy in prepubertal rat testes induced by joint exposure of bisphenol A and nonylphenol. *Environ Pollut*. 2018;243:693–702. <https://doi.org/10.1016/j.envpol.2018.09.030>.
  71. Chen L, Zhang X, Zhang Q, et al. A necroptosis related prognostic model of pancreatic cancer based on single cell sequencing analysis and transcriptome analysis. *Front Immunol*. 2022. <https://doi.org/10.3389/fimmu.2022.1022420>.
  72. Chen X, Chen X, Huang Y, Lin J, Wu Y, Chen Y. TCP1 increases drug resistance in acute myeloid leukemia by suppressing autophagy via activating AKT/mTOR signaling. *Cell Death Dis*. 2021. <https://doi.org/10.1038/s41419-021-04336-w>.
  73. Wang M, Zhang G, Zhang Y, et al. Fibrinogen alpha chain knockout promotes tumor growth and metastasis through integrin-AKT signaling pathway in lung cancer. *Mol Cancer Res*. 2020;18(7):943–54. <https://doi.org/10.1158/1541-7786.mcr-19-1033>.
  74. Chi NF, Chang TH, Lee CY, et al. Untargeted metabolomics predicts the functional outcome of ischemic stroke. *J Formos Med Assoc*. 2021;120(1):234–41. <https://doi.org/10.1016/j.jfma.2020.04.026>.
  75. Hou JY, Cao GZ, Tian LL, et al. Integrated transcriptomics and metabolomics analysis reveals that C3 and C5 are vital targets of DuZhi Wan in protecting against cerebral ischemic injury. *Biomed Pharm*. 2022;155:113703. <https://doi.org/10.1016/j.biopha.2022.113703>.
  76. Luo A, Zhou X, Shi X, et al. Exosome-derived miR-339-5p mediates radiosensitivity by targeting Cdc25A in locally advanced esophageal squamous cell carcinoma. *Oncogene*. 2019;38(25):4990–5006. <https://doi.org/10.1038/s41388-019-0771-0>.
  77. Lu J, Liu QH, Wang F, et al. Exosomal miR-9 inhibits angiogenesis by targeting MDK and regulating PDK/AKT pathway in nasopharyngeal carcinoma. *J Exp Clin Cancer Res*. 2018. <https://doi.org/10.1186/s13046-018-0814-3>.
  78. Maity J, Barthels D, Sarkar J, et al. Ferutinin induces osteoblast differentiation of DPSCs via induction of KLF2 and autophagy/mitophagy. *Cell Death Dis*. 2022. <https://doi.org/10.1038/s41419-022-04903-9>.
  79. Liu X, Xu C, Xu L, et al. Empagliflozin improves diabetic renal tubular injury by alleviating mitochondrial fission via AMPK/SP1/PGLAM5 pathway. *Metabolism*. 2020;111: 154334. <https://doi.org/10.1016/j.metabol.2020.154334>.
  80. Wu Z, Huang H, Han Q, et al. SENP7 senses oxidative stress to sustain metabolic fitness and antitumor functions of CD8+ T cells. *J Clin Invest*. 2022. <https://doi.org/10.1172/jci155224>.
  81. Zhu Y, Liu Z, Wan Y, et al. PARP14 promotes the growth and glycolysis of acute myeloid leukemia cells by regulating HIF-1 $\alpha$  expression. *Clin Immunol*. 2022;242: 109094. <https://doi.org/10.1016/j.clim.2022.109094>.
  82. McGovern JA, Bock N, Shafiee A, et al. A humanized orthotopic tumor microenvironment alters the bone metastatic tropism of prostate cancer cells. *Commun Biol*. 2021. <https://doi.org/10.1038/s42003-021-02527-x>.
  83. Zhao F, Wang M, Li S, et al. DACH1 inhibits SNAI1-mediated epithelial-mesenchymal transition and represses breast carcinoma metastasis. *Oncogenesis*. 2015;4(3):e143–e143. <https://doi.org/10.1038/oncsis.2015.3>.
  84. Alhabbal A, Abou KI. Immunohistochemical analysis of intestinal biopsies in individuals with celiac disease. *JGH Open*. 2022;6(10):692–5. <https://doi.org/10.1002/jgh3.12807>.
  85. Zhang QF, Li J, Jiang K, et al. CDK4/6 inhibition promotes immune infiltration in ovarian cancer and synergizes with PD-1 blockade in a B cell-dependent manner. *Theranostics*. 2020;10(23):10619–33. <https://doi.org/10.7150/thno.44871>.

## Publisher's Note

Springer Nature remains neutral with regard to jurisdictional claims in published maps and institutional affiliations.